

# Holographic deep thermalization: theory and experimentation

Bingzhi Zhang,<sup>1,2,\*</sup> Peng Xu,<sup>3,†</sup> Xiaohui Chen,<sup>4</sup> and Quntao Zhuang<sup>2,1,‡</sup>

<sup>1</sup>*Department of Physics and Astronomy, University of Southern California, Los Angeles, California 90089, USA*

<sup>2</sup>*Ming Hsieh Department of Electrical and Computer Engineering,  
University of Southern California, Los Angeles, California 90089, USA*

<sup>3</sup>*Department of Statistics, University of Illinois at Urbana-Champaign, Champaign, IL 61820, USA*

<sup>4</sup>*Department of Mathematics, University of Southern California, Los Angeles, California 90089, USA*

Randomness is a cornerstone of science, underpinning fields such as statistics, information theory, dynamical systems, and thermodynamics. In quantum science, quantum randomness, especially random pure states, plays a pivotal role in fundamental questions like black hole physics and quantum complexity, as well as in practical applications such as quantum device benchmarking and quantum advantage certification. The conventional approach for generating genuine random states, called ‘deep thermalization’, faces significant challenges, including scalability issues due to the need for a large ancilla system and susceptibility to attacks, as demonstrated in this work. We introduce holographic deep thermalization, a secure and hardware-efficient quantum random state generator. By adopting a sequential application of a scrambling-measure-reset process, it continuously trades space with time, and substantially reduces the required ancilla size to as small as a system-size independent constant; At the same time, it guarantees security by removing quantum correlation between the data system and attackers. Thanks to the resource reduction, our circuit-based implementation on IBM Quantum devices achieves genuine 5-qubit random state generation utilizing only a total of 8 qubits.

Randomness is a fundamental concept in science, underpinning the backbone of fields such as statistics, information theory, dynamical systems, and thermodynamics. Its applications are extensive, spanning cryptography, Monte Carlo simulations, and machine learning. True randomness originates from quantum physics, where the act of measurement collapses quantum superpositions into inherently unpredictable outcomes. Random quantum states, in particular, have become central to modern quantum science, playing a crucial role in understanding foundational theories, such as black hole physics [1], quantum chaos [2], and the complexity of quantum circuits [3]. Random quantum states are equally essential in practical applications, including quantum device benchmarking [4], quantum advantage certification [5, 6], quantum cryptography [7] and quantum learning [8, 9]. The unique type of random quantum states necessary in these scenarios is the Haar random ensemble uniformly distributed over the entire Hilbert space, which represents typical quantum states with high complexity and volume-law entanglement. For the same reason, though, Haar ensemble is also difficult to sample from.

Several approaches have been developed to generate approximate Haar random states. Early approach of local random unitary circuits requires a large depth linear in system size [10, 11]. In addition, generating different samples is achieved by randomly adjusting the quantum gates, leading to significant overhead in quantum circuit compilation and experimentation. More importantly, such an approach only generates pseudo-random quan-

tum states, as the classical random numbers involved are typically pseudo-random.

Recently, *deep thermalization* (DT) [12–15] suggests a promising approach to generate genuine random states from partial quantum measurements, with both initial state and quantum dynamics fixed. Random states emerge within a small subsystem via projective measurements over the rest when the whole system sufficiently thermalizes. However, such approaches require a large number of ancilla qubits linearly growing with the system size, casting an experimental challenge considering near-term quantum devices [15]. Furthermore, we prove that DT is vulnerable to entanglement attack—initial quantum correlation between the data system and attacker decays at most by a constant regardless of ancilla size.

In this work, we introduce the *holographic deep thermalization* (HDT), a secure and hardware-efficient paradigm for generating random quantum states with only a *constant* number of ancilla qubits, via trading space resource with time [16]. In each time step, a fixed unitary with high-complexity, similar to that in DT yet on a much smaller system, is applied and then the constant number of ancillae are measured and reset. We rigorously prove the convergence of HDT in terms of the frame potential and show that quantum correlation between the data system and any attacker is erased step-by-step to guarantee security. Thanks to the resource reduction, our circuit-based implementation on IBM Quantum devices achieves genuine 2-qubit random state generation utilizing only a 4-qubit system, while previous work adopts a 10-atom system [15]. When adopting 5 data qubits and 3 ancilla qubits, we also extend the dimension of random states to  $d_A = 32$ , representing a six-fold increase compared to the previous experiment [15].

Furthermore, via balancing the ancilla size and num-

\* These two authors contributed equally.; bingzhiz@usc.edu

† These two authors contributed equally.

‡ qzhuang@usc.edu

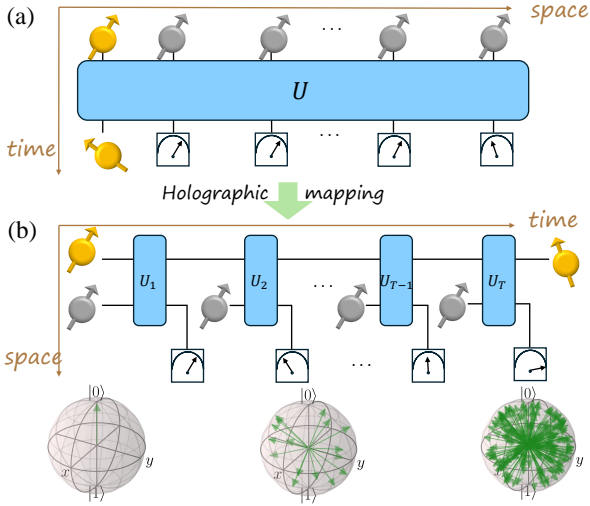


Figure 1. Conceptual plot of (a) deep thermalization with a single chaotic unitary  $U$  and (b) holographic deep thermalization with a sequence of chaotic unitaries  $\{U_t\}_{t=1}^T$ . Yellow and gray represents data and ancilla systems.

ber of time steps, HDT achieves a continuous trade-off between the total quantum circuit size and the ancilla size, as we demonstrate analytically and experimentally. Besides the minimum-space operating point, we also identify a minimum-quantum-circuit-size operating point where ancilla size equals the system size.

### Problem set-up and protocol design

Generation of genuinely quantum random states in DT relies on quantum measurement projection. For a fixed pure quantum state  $|\Psi\rangle_{AB}$  on a joint system of data  $A$  and ancilla  $B$ , the *projected ensemble*  $\mathcal{E}(\Psi)$  on subsystem  $A$  is generated via a projective measurement on subsystem  $B$ , e.g., with projectors  $\{|z\rangle\langle z|_B\}$  in the computational basis [13]. Conditioned on the measurement result  $z$  on  $B$ , data system  $A$  results in a pure state  $|\psi_z\rangle \propto {}_B\langle z|\Psi\rangle_{AB}$ , with probability  $p_z = \text{tr}(|\Psi\rangle\langle\Psi|_{AB} |z\rangle\langle z|_B)$ .

To quantify the closeness of a state ensemble  $\mathcal{E}(\Psi)$  to the Haar random ensemble up to the  $K$ -th moment, we consider its frame potential [14], defined as

$$\begin{aligned} \mathcal{F}^{(K)} &\equiv \sum_{z,z'} p_z p_{z'} |\langle \psi_z | \psi_{z'} \rangle|^{2K} \\ &\geq \mathcal{F}_{\text{Haar}}^{(K)} = \binom{d_A + K - 1}{d_A - 1}^{-1}, \end{aligned} \quad (1)$$

where  $d_A = 2^{N_A}$  is the dimension of the  $N_A$ -qubit data system  $A$ . The frame potential quantifies the inversely occupied symmetric space dimension and is thus lower bounded by the value of Haar ensemble  $\mathcal{F}_{\text{Haar}}^{(K)}$ .

When an ensemble achieves the minimum frame potential  $\mathcal{F}_{\text{Haar}}^{(K)}$ , one regards the ensemble as the  $K$ -design [2, 12–14], which approximates the Haar random ensemble to at least the  $K$ -th moment. An  $\epsilon$ -approximate  $K$ -

design state ensemble  $\mathcal{E}$  is defined via the relative deviation of frame potential as  $\delta^{(K)} \equiv \mathcal{F}^{(K)}/\mathcal{F}_{\text{Haar}}^{(K)} - 1 \leq \epsilon$  [17].

Previous studies on the conventional DT [12–14] (cf. Fig. 1a) focused on the projected ensemble obtained from a single fixed unitary on a trivial initial state. It requires  $N_B = \Omega(KN_A + \log(1/\epsilon))$  ancilla qubits to achieve the  $\epsilon$ -approximate  $K$ -design [13], which creates an overhead growing with the system size and especially for high-order state design generation.

We propose HDT (cf. Fig. 1b), which extends the time direction to  $T$  discrete steps to compensate for the reduction in space resource—in the same spirit of holographic quantum simulation [16]. HDT also begins with a trivial state, e.g.,  $|\psi_0\rangle = |0\rangle^{\otimes N_A}$ . In each of the  $T$  time steps,  $N_B$  ancilla qubits initialized in  $|0\rangle^{\otimes N_B}$  interact with data system  $A$  through a fixed unitary  $U_t$  with high-complexity, which can be implemented by either a randomly sampled fixed deep quantum circuit [18, 19] or chaotic Hamiltonian evolution [12, 13]. Following projective measurements on the ancilla system, the *projected ensemble*  $\mathcal{E}_t$  of the data system at step  $t$  is fed towards the next time step as input.

### Convergence towards the Haar ensemble

Assuming that each  $U_t$  is a typical unitary, one expects the *projected ensemble*  $\mathcal{E}_t$  to converge towards the fixed point of Haar ensemble, as  $T$  increases. Indeed, our HDT only requires  $K + \log_2(1/\epsilon)$  constant number of ancilla qubits and a time step of  $KN_A/[K + \log_2(1/\epsilon)]$  to achieve  $\epsilon$ -approximate  $K$ -design.

Below, we evaluate the frame potential to quantify the rate of convergence. Denoting the data and ancilla system dimension as  $d_A = 2^{N_A}$  and  $d_B = 2^{N_B}$ , we begin with exact solution for the typical first-order frame potential (see Appendix C for proof).

**Theorem 1** *The typical first-order frame potential  $\mathcal{F}^{(1)}(t)$  of the projected ensemble  $\mathcal{E}_t$  at step  $t$  in the holographic deep thermalization is*

$$\begin{aligned} \mathcal{F}^{(1)}(t) &= \frac{(d_A - 1)(d_A d_B - 1)}{d_A^2 d_B + 1} \left( \frac{(d_A^2 - 1)d_B}{d_A^2 d_B^2 - 1} \right)^t \\ &\quad + \frac{d_A^2 (d_B + 1)}{d_A^2 d_B + 1} \mathcal{F}_{\text{Haar}}^{(1)}. \end{aligned} \quad (2)$$

*In the thermodynamic limit of data system  $d_A \rightarrow \infty$ , we have  $\mathcal{F}^{(1)}(t) \simeq (1 + 1/d_B) \mathcal{F}_{\text{Haar}}^{(1)} + d_B^{-t}$ .*

The results are derived by representing the typical case of  $\{U_t\}$  with Haar expectation values due to self-averaging (see Appendix. F), in the same spirit of Refs. [13, 14].

We numerically (red dots) and experimentally (blue circles) verify Eq. (2) (light red solid) in Fig. 2a. The experiment on IBM quantum devices, with  $N_A = 2, N_B = 2$  and up to  $t = 8$  steps, demonstrates a good agreement with the theory up to some additional decay from decoherence noise.

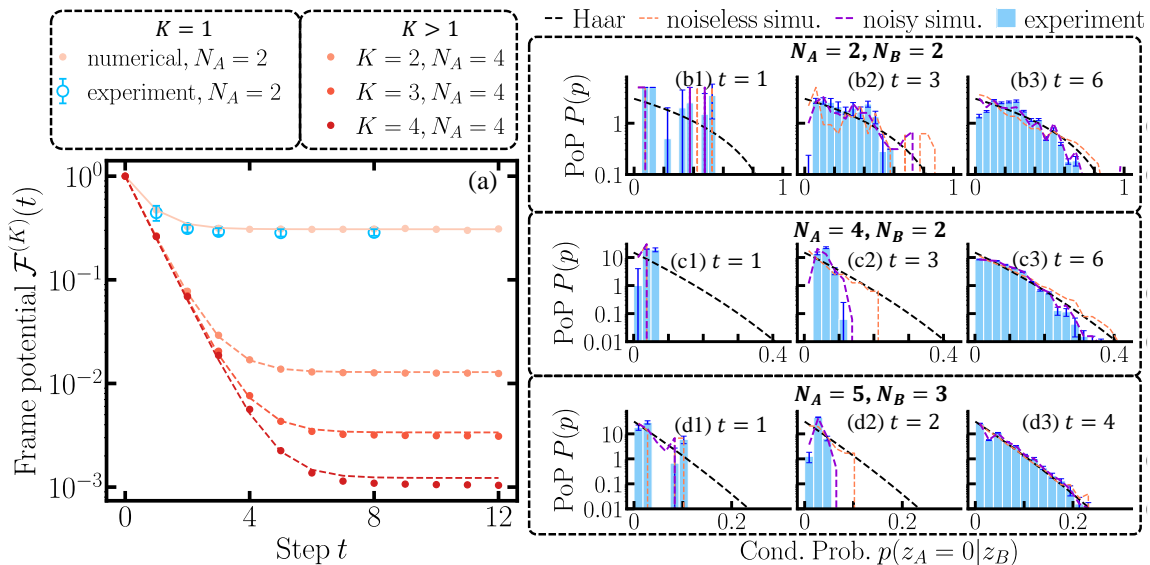


Figure 2. Dynamics of frame potential and probability distribution of probability (PoP) of *projected ensemble* in HDT. In (a), the red dots and from light to dark represent numerical simulation results of  $\mathcal{F}^{(K)}(t)$  in HDT from  $K = 1$  to  $K = 4$  with  $N_B = 2$ . The red solid line represents first-order theoretical prediction of Eq. (2) in Theorem 1 and red dashed lines from light to dark represent higher-order theory in Eq. (3) for corresponding  $K$ . Blue dots with errorbars show IBM Quantum experimental results for  $\mathcal{F}^{(1)}(t)$ . In the right panel, we plot the PoP at different time steps in HDT with various choices of data and ancilla system  $N_A, N_B$  (listed in titles). Blue bars represent the IBM Quantum experimental results of average PoP with errorbars indicating fluctuations. Black dashed lines are PT distribution for Haar theory, orange and purple dashed lines show the noiseless and noisy simulations of device for reference.

For higher-order frame potentials, we have the following result.

**Result 2** *The typical  $K$ -th frame potential  $\mathcal{F}^{(K)}(t)$  ( $K > 1$ ) of the projected ensemble  $\mathcal{E}_t$  at step  $t$  in the holographic deep thermalization is asymptotically ( $d_A \gg 1$ )*

$$\mathcal{F}^{(K)}(t) \simeq \left( \frac{d_A^2 d_B}{d_A^2 d_B^2 - 1} \right)^t + \left( 1 + \frac{2^K - 1}{d_B} \right) \mathcal{F}_{\text{Haar}}^{(K)}. \quad (3)$$

The first dynamical term is obtained in Appendix A as a rigorous lower bound; While the second constant term combines numerical observation and the analytical result for  $K = 1$  in Theorem 1, the form of the solution in Eq. (3) can be obtained under reasonable assumptions, as we present in Appendix C. In Fig. 2a, the dynamical solution in Eq. (3) (red dashed lines) aligns with the numerical results (dots) and thus captures the convergence dynamics of higher-order frame potentials.

We next turn to an efficiently-measurable signature of randomness adopted in the study of quantum device characterization and benchmarking [5, 20]—the *probability distribution of probability* (PoP), which describes the distribution of the state overlap between the ensemble and an arbitrary fixed quantum states  $|\phi\rangle$ . For Haar random ensemble, the PoP is known to follow the Porter-Thomas (PT) distribution [20, 21],  $P_{|\psi\rangle \in \text{Haar}} \left[ |\langle \phi | \psi \rangle|^2 = p \right] \propto (1-p)^{d_A-2}$ . We experimentally measure the PoP of the *projected ensemble* through

HDT at various time steps in Fig. 2b-d, and compare to PT distribution (black dashed line). At early stage  $t = 1$ , the measured PoP (light blue) differs significantly from the PT distribution (black dashed) as expected due to limited measurements, while with iterative evolution and measurements, the histogram converges towards the PT distribution, consistent with the numerical simulation with hardware noise (purple dashed). From subplots b,c to d, the agreement with Haar theory improves when  $N_A$  increases from 2, 4, to 5, due to finite-system size effect being mitigated, as the noiseless simulation (orange dashed) indicates. Compared with previous conventional DT experiment limited to randomizing  $d_A = 5$  dimensional data system with a total of 10 atoms on analog simulator [15], the drastic resource reduction of HDT allows the extension to  $d_A = 32$  dimensional data system ( $N_A = 5$ ) with a total of only 8 qubits.

### Space-time trade-off

Here, we analyze the space-time trade-off in details, assuming that each unitary  $U_t$  is implemented via a gate-based local quantum circuit. We will also consider the large system size limit  $d_A \gg 1$  to simplify expressions, although this approximation is not essential. From Theorem 1 for  $K = 1$  and Eq. (3) for  $K \geq 2$ , HDT only needs a constant number of  $N_B \gtrsim K + \log_2(1/\epsilon)$  ancilla qubits to generate an  $\epsilon$ -approximate  $K$ -design state ensemble, given enough number of steps. Assuming that  $N_B \gtrsim K + \log_2(1/\epsilon)$ , due to the fast exponential con-

vergence of  $\propto d_B^{-t}$  regardless of order  $K$ , the necessary number of time steps for convergence in  $K$ -th order becomes

$$N_B \times T \gtrsim KN_A - \log_2(K!) + \log_2\left(\frac{1}{\epsilon}\right), \quad (4)$$

leading to the trade-off between space — the number of ancilla  $N_B$  — and time step  $T$ , hence the name ‘holographic deep thermalization’. To reach the same performance on  $N_A$  qubits, the space-time product  $N_B \times T$  is roughly constant. Note that conventional DT corresponds to  $T = 1$ , which requires an ancilla size  $N_B \gtrsim KN_A + \log_2(1/\epsilon)$ , compared to the minimum constant number ancillae  $N_B \gtrsim K + \log_2(1/\epsilon)$  in the HDT.

The space-time trade-off can be most easily verified by data collapse when introducing a rescaled time  $\tau \simeq tN_B$  and the rescaled frame potential  $f^{(K)}(t) = \mathcal{F}^{(K)}(t)/\mathcal{F}^{(K)}(\infty)$ . Via the rescaling, the typical frame potentials of HDT with different ancilla size  $N_B$  collapse to  $f^{(K)}(\tau) \simeq 1 + 2^{-\tau}/\mathcal{F}_{\text{Haar}}^{(K)}$ , indicated by the black dashed curves in Fig. 3ab. Indeed, our numerical results (Fig. 3ab) for various choices of  $N_B$  all collapse to the theory prediction with slight deviations due to limited  $d_A$ , verifying the space-time trade-off. With increasing ancilla size  $N_B$  and time steps  $t$ , we see an alignment in the monotonic decrease of relative frame potential deviation  $\delta^{(1)}(T)$  between Haar theory and experiment in Fig. 3cd. The rescaled frame potential of experiments (blue triangles in Fig. 3a) also approximately collapses, confirming the universal scaling law.

In a gate-based realization of HDT, each unitary  $U_t$  requires at least  $\propto (N_A + N_B)$  layers of quantum circuits and therefore  $\propto (N_A + N_B)^2$  gates in order to represent a fixed typical unitary from  $K$ -design. Thus, a more comprehensive way of quantifying the spacetime resource is via the quantum circuit size — the total number of gates — Q-size  $\propto (N_A + N_B)^2 T$ . From Ineq. (4), we can perform asymptotic analyses of Q-size, as detailed in Appendix E. Fig. 3e summarizes the tradeoff for large systems  $N_A \gg K \log_2(1/\epsilon)$  and the common case of  $K < \log_2(1/\epsilon)$ : the minimum quantum circuit size Q-size  $\propto 4KN_A^2$  is achieved at  $N_B = N_A$ , as indicated by the red triangle. Meanwhile, in conventional DT corresponding to  $T = 1$  with  $N_B = KN_A + \log_2(1/\epsilon)$ , we have Q-size  $\propto (K + 1)^2 N_A^2$ , as indicated by the orange dot. For the minimum space (ancilla) case of  $N_B \sim K + \log_2(1/\epsilon)$ , the quantum circuit size grows as  $KN_A^3/(K + \log_2(1/\epsilon))$ .

### Security of quantum randomness

An important property of true randomness is that it cannot be predicted prior to generation. In the classical world, prediction of random number means that a sequence of classical number  $\mathbf{X}$  is chosen and fixed prior to the generation of random number  $\mathbf{Y}$ . In multiple experiments, if the correlation measured by mutual information  $I(\mathbf{X} : \mathbf{Y})$  is large, then  $\mathbf{X}$  can infer random number  $\mathbf{Y}$ . In a lottery scenario, this means one can cheat to win the prize. In the quantum case, we can generalize such

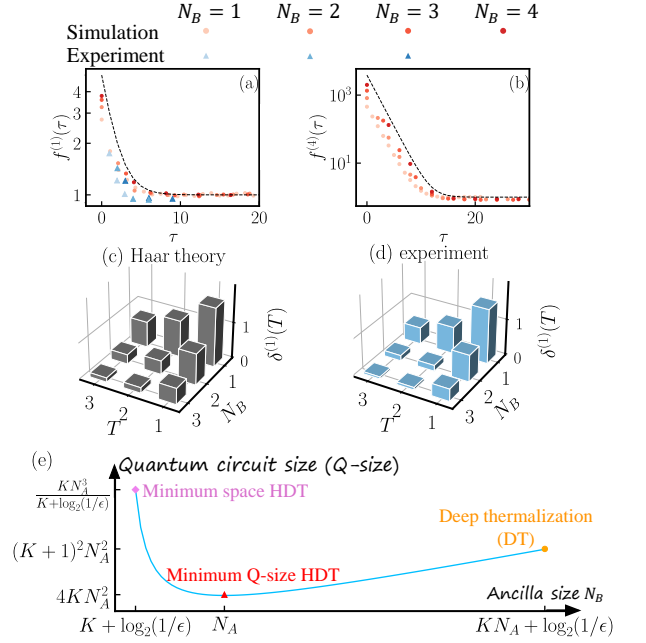


Figure 3. Space-time trade-off in HDT. The rescaled frame potential dynamics for (a)  $K = 1$ ,  $N_A = 2$  and (b)  $K = 4$ ,  $N_A = 4$  versus a rescaled time, indicating a universal scaling over different ancilla size  $N_B$  (light to dark red dots). Black dashed lines represent the theoretical asymptotic universal scaling as  $f^{(K)}(\tau) \simeq 1 + 2^{-\tau}/\mathcal{F}_{\text{Haar}}^{(K)}$ . In the central panel, we plot the relative deviation of frame potential  $\delta^{(1)}(T) = \mathcal{F}^{(1)}(T)/\mathcal{F}_{\text{Haar}}^{(1)}(T) - 1$  versus ancilla size  $N_B$  and evolution steps  $T$  for (c) Haar theory and (d) experimental results. The decrease of the relative deviation  $\delta^{(1)}(T)$  reveals the space-time trade-off as  $N_B T \gtrsim \text{const}$ . The corresponding rescaled  $f^{(1)}(\tau)$  of experiments are shown by light to dark blue triangles in (a) for  $N_B = 1, 2, 3$ . (e) Quantum circuit size of HDT in generating  $\epsilon$ -approximate  $K$ -design versus ancilla size for large system  $N_A \gg K \log_2(1/\epsilon)$  assuming  $K < \log_2(1/\epsilon)$ . Orange circle represent conventional DT, which also corresponds to  $T = 1$  in HDT. Red triangle and violet diamond represent Q-size in HDT with minimum Q-size and minimum space separately. The labels on  $y$ -axis represent the scaling of Q-size from Eq. (E3).

a notion by introducing a reference quantum system  $R$ . Under the condition that no quantum operation can be performed on  $R$  after random number generation process starts, we regard the quantum randomness as insecure if the quantum mutual information between  $R$  and the final random quantum system  $A_{\text{out}}$  is large. For example, if  $RA_{\text{out}}$  is eventually in the maximally-entangled Bell states, then any measurement on  $A_{\text{out}}$  and  $R$  agrees and the ‘quantum lottery’ is hacked.

We can consider a particular attack based on entanglement engineering. As shown in Fig. 4a, the attack engineers the reference  $R$  and the initial data system  $A_{\text{in}}$  in the maximally entangled Bell state. In a DT process (shown in a1), the data system interacts with the large ancilla  $B$ ; while in the HDT process (shown

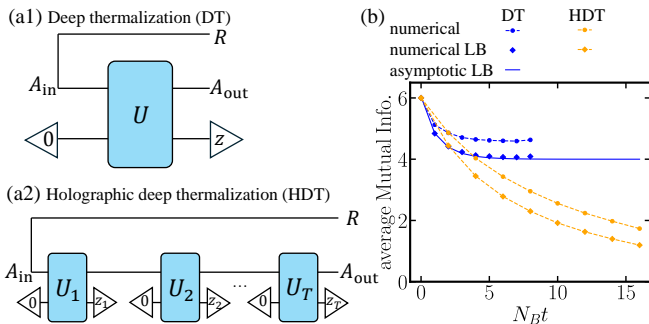


Figure 4. Dynamics of average mutual information. We show conceptual plot for mutual information measure in (a1) deep thermalization (DT) and (a2) holographic deep thermalization (HDT). The input data system is initially maximally entangled with a reference system  $R$ . In (b), we plot the dynamics of trajectory-average mutual information (dots) and its Rényi lower bound (diamonds) versus  $N_B t$ . The blue solid line is the theory of Eq. (5) in Lemma 3. In DT, we enlarge ancilla system  $N_B$  holding  $t = 1$ , and in HDT, we fix  $N_B = 2$  but extend evolution steps  $t$ . In both cases, the data system consists of  $N_A = 3$  qubits.

in a2), the data system repetitively interacts with the ancilla via measurement and reset. We evaluate the expected quantum mutual information averaged over the measurement results  $\mathbf{z} = (z_1, \dots, z_T)$ ,  $\mathbb{E}_{\mathbf{z}} I(R : A_{\text{out}} | \mathbf{z}) = \mathbb{E}_{\mathbf{z}} 2S(A_{\text{out}} | \mathbf{z})$  for both DT and HDT, where  $S(\cdot)$  is the von-Neumann entropy. When further averaged over the Haar ensemble to represent the typical case, we obtain the following results, with proof in Appendix D.

**Lemma 3** *The typical quantum mutual information averaged over the measurement results in deep thermalization only decrease by at most 2, regardless of ancilla size. More precisely, it can be asymptotically ( $d_A \gg 1$ ) lower bounded,*

$$\begin{aligned} \mathbb{E}_{\mathbf{z}} [I(R : A_{\text{out}} | \mathbf{z})] &\geq \mathbb{E}_{\mathbf{z}} [2S_2(A_{\text{out}} | \mathbf{z})] \\ &\gtrsim 2(N_A - 1) - 2 \log_2 \left( 1 - \frac{1}{2d_B} - \frac{1}{2d_A^2 d_B} \right), \end{aligned} \quad (5)$$

where  $S_2(A_{\text{out}} | \mathbf{z})$  is the Rényi-2 entropy of reduced state  $\text{tr}_R(|\psi_{\mathbf{z}}\rangle\langle\psi_{\mathbf{z}}|_{RA_{\text{out}}})$  conditioned on measurement result  $\mathbf{z}$ .

In Fig. 4b, the numerical results of average mutual information  $\mathbb{E}_{\mathbf{z}} [I(R : A_{\text{out}} | \mathbf{z})]$  (dots) decay synchronously with the Rényi lower bound  $\mathbb{E}_{\mathbf{z}} [2S_2(A_{\text{out}} | \mathbf{z})]$  (diamonds) in DT (blue) and HDT (orange), indicating a well-behaved numerically-evaluated lower bound. Moreover, the numerical results of DT lower bound (blue diamonds) agree with the analytical lower bound (blue solid line) in Ineq. (5), which only decays by less than 2. On the contrary, HDT allows the continuous decrease of mutual information (orange dots and diamonds) towards zero, as

the number of time steps increases, converging towards secure quantum randomness independent of the reference system.

## Discussions

In conclusion, we have proposed HDT for genuine quantum random states generation, and have shown the convergence dynamics of output states to Haar ensemble, and its robustness against entanglement attack in contrast to conventional DT. Moreover, we have shown the emergent space-time trade-off in HDT and identified the optimal configuration meeting minimum resource requirement. The proposed HDT protocol can be further enhanced by generative quantum machine learning. As we detail in Appendix A, parameterizing and training the unitaries in each step enables a constant-factor improved convergence. Our model can also be regarded as a generalized monitored circuit with fixed measurement rate and location, which provides insights for the understanding of complexity growth in the monitored circuit beyond entanglement growth transition [22].

We point out some future directions. The rigorous proof for the dynamics of higher-order frame potential is subject to a future study for a complete theoretical understanding. It is also an open direction to explore Hamiltonian-dynamics version of HDT, where both infinite-temperature and finite-temperature [23], unconstrained and constrained (e.g., symmetry [24] or quantum many-body scar [25]) can be considered.

Another intriguing direction is to establish the rigorous notion of security in quantum random state generation. While quantum random number generation concerns about the generation of classical random numbers from quantum device [26–28], the security of random quantum state generation is less explored. The study of computational pseudo-random quantum state focuses on the closeness to Haar [29, 30], while in our case we are concerned about the device-level attack. The information security paradigm in DT and HDT can also be explored as an extension of Hayden-Preskill protocol [1] to study the intersection between quantum measurements and black hole information paradox.

**Acknowledgments.** BZ thanks Matteo Ippoliti for discussions, BZ and PX thank Runzhe Mo for suggestions on the experiment. QZ and BZ acknowledge support from NSF (CCF-2240641, OMA-2326746, 2350153), ONR N00014-23-1-2296, AFOSR MURI FA9550-24-1-0349 and DARPA (HR0011-24-9-0362, HR00112490453, HR001123S0052). XC and PX acknowledge support from NSF (DMS-2413404, 2347760). This work was partially funded by an unrestricted gift from Google and a gift from the Simons Foundation. The experiment was conducted using IBM Quantum Systems provided through USC’s IBM Quantum Innovation Center.

- 
- [1] P. Hayden and J. Preskill, *Journal of high energy physics* **2007**, 120 (2007).
- [2] D. A. Roberts and B. Yoshida, *Journal of High Energy Physics* **2017**, 1 (2017).
- [3] F. G. Brandão, W. Chemissany, N. Hunter-Jones, R. Kueng, and J. Preskill, *PRX Quantum* **2**, 030316 (2021).
- [4] A. W. Cross, L. S. Bishop, S. Sheldon, P. D. Nation, and J. M. Gambetta, *Physical Review A* **100**, 032328 (2019).
- [5] F. Arute, K. Arya, R. Babbush, D. Bacon, J. C. Bardin, R. Barends, R. Biswas, S. Boixo, F. G. Brandao, D. A. Buell, *et al.*, *Nature* **574**, 505 (2019).
- [6] M. Tillmann, B. Dakić, R. Heilmann, S. Nolte, A. Szameit, and P. Walther, *Nature photonics* **7**, 540 (2013).
- [7] S. Pirandola, U. L. Andersen, L. Banchi, M. Berta, D. Bunandar, R. Colbeck, D. Englund, T. Gehring, C. Lupo, C. Ottaviani, *et al.*, *Advances in optics and photonics* **12**, 1012 (2020).
- [8] H.-Y. Huang, R. Kueng, and J. Preskill, *Nature Physics* **16**, 1050 (2020).
- [9] A. Elben, S. T. Flammia, H.-Y. Huang, R. Kueng, J. Preskill, B. Vermersch, and P. Zoller, *Nature Reviews Physics* **5**, 9 (2023).
- [10] F. G. Brandao, A. W. Harrow, and M. Horodecki, *Communications in Mathematical Physics* **346**, 397 (2016).
- [11] A. W. Harrow and S. Mehraban, *Communications in Mathematical Physics*, 1 (2023).
- [12] W. W. Ho and S. Choi, *Physical Review Letters* **128**, 060601 (2022).
- [13] J. S. Cotler, D. K. Mark, H.-Y. Huang, F. Hernandez, J. Choi, A. L. Shaw, M. Endres, and S. Choi, *PRX quantum* **4**, 010311 (2023).
- [14] M. Ippoliti and W. W. Ho, *PRX Quantum* **4**, 030322 (2023).
- [15] J. Choi, A. L. Shaw, I. S. Madjarov, X. Xie, R. Finkelstein, J. P. Covey, J. S. Cotler, D. K. Mark, H.-Y. Huang, A. Kale, *et al.*, *Nature* **613**, 468 (2023).
- [16] S. Anand, J. Hauschild, Y. Zhang, A. C. Potter, and M. P. Zaletel, *PRX Quantum* **4**, 030334 (2023).
- [17] It is in fact equivalent to the definition by the normalized moment distance (cf. Appendix B).
- [18] A. Nahum, J. Ruhman, S. Vijay, and J. Haah, *Physical Review X* **7**, 031016 (2017).
- [19] A. Nahum, S. Vijay, and J. Haah, *Physical Review X* **8**, 021014 (2018).
- [20] S. Boixo, S. V. Isakov, V. N. Smelyanskiy, R. Babbush, N. Ding, Z. Jiang, M. J. Bremner, J. M. Martinis, and H. Neven, *Nature Physics* **14**, 595 (2018).
- [21] C. E. Porter and R. G. Thomas, *Physical Review* **104**, 483 (1956).
- [22] B. Skinner, J. Ruhman, and A. Nahum, *Physical Review X* **9**, 031009 (2019).
- [23] D. K. Mark, F. Surace, A. Elben, A. L. Shaw, J. Choi, G. Refael, M. Endres, and S. Choi, *arXiv preprint arXiv:2403.11970* (2024).
- [24] N. D. Varikuti and S. Bandyopadhyay, *arXiv preprint arXiv:2402.08949* (2024).
- [25] T. Bhore, J.-Y. Desaulles, and Z. Papić, *Physical Review B* **108**, 104317 (2023).
- [26] U. Vazirani and T. Vidick, in *Proceedings of the forty-fourth annual ACM symposium on Theory of computing* (2012) pp. 61–76.
- [27] Z. Cao, H. Zhou, X. Yuan, and X. Ma, *Physical Review X* **6**, 011020 (2016).
- [28] D. Drahi, N. Walk, M. J. Hoban, A. K. Fedorov, R. Shakhovoy, A. Feimov, Y. Kurochkin, W. S. Kolthammer, J. Nunn, J. Barrett, *et al.*, *Physical Review X* **10**, 041048 (2020).
- [29] Z. Ji, Y.-K. Liu, and F. Song, in *Advances in Cryptology—CRYPTO 2018: 38th Annual International Cryptology Conference, Santa Barbara, CA, USA, August 19–23, 2018, Proceedings, Part III 38* (Springer, 2018) pp. 126–152.
- [30] P. Ananth, L. Qian, and H. Yuen, in *Annual International Cryptology Conference* (Springer, 2022) pp. 208–236.
- [31] Qiskit contributors, *Qiskit: An open-source framework for quantum computing* (2023).
- [32] A. Kandala, A. Mezzacapo, K. Temme, M. Takita, M. Brink, J. M. Chow, and J. M. Gambetta, *nature* **549**, 242 (2017).
- [33] B. Zhang, P. Xu, X. Chen, and Q. Zhuang, *Physical Review Letters* **132**, 100602 (2024).
- [34] S.-X. Zhang, J. Allcock, Z.-Q. Wan, S. Liu, J. Sun, H. Yu, X.-H. Yang, J. Qiu, Z. Ye, Y.-Q. Chen, *et al.*, *Quantum* **7**, 912 (2023).
- [35] M. Ippoliti and W. W. Ho, *Quantum* **6**, 886 (2022).
- [36] P. W. Claeys and A. Lamacraft, *Quantum* **6**, 738 (2022).
- [37] F. G. Brandão, A. Kalev, T. Li, C. Y.-Y. Lin, K. M. Svore, and X. Wu, *arXiv:1710.02581* (2017).
- [38] M. Cerezo, A. Sone, J. L. Beckey, and P. J. Coles, *Quantum Science and Technology* **6**, 035008 (2021).

## Appendix A: Details of simulation and experiments

### 1. Preliminary and results for state design

Statistical properties of a quantum state ensemble  $\mathcal{E}(\Psi) = \{|\psi_z\rangle, p_z\}$  are characterized by its  $K$ -th moment ( $K \geq 1$ ), which is captured by the  $K$ -th moment operator of ensemble [2, 12–14],

$$\rho^{(K)} = \sum_z p_z (|\psi_z\rangle\langle\psi_z|)^{\otimes K}. \quad (\text{A1})$$

Specifically, for Haar ensemble in Hilbert space of dimension  $d_A$ , the moment operator

$$\rho_{\text{Haar}}^{(K)} = \frac{\sum_{\pi \in S_K} \hat{\pi}}{\prod_{i=0}^{K-1} (d_A + i)} = \Pi_K \begin{pmatrix} K + d_A - 1 \\ d_A - 1 \end{pmatrix}^{-1}, \quad (\text{A2})$$

where  $S_K$  is the symmetric group on a  $K$ -element set,  $\hat{\pi}$  is the operator representation of permutation on  $\mathcal{H}^{\otimes K}$ , and  $\Pi_K = \sum_{\pi \in S_K} \hat{\pi} / K!$  is the projector onto the symmetric subspace.

In the main text, we adopted the frame potential to quantify the closeness to Haar state ensemble, which also equals the purity of the moment operator,  $\mathcal{F}^{(K)} = \text{tr}[\rho^{(K)2}]$ . One can show that the relative deviation in frame potential is equivalent to the normalized moment distance with  $\|\cdot\|_2$  denoting Schatten-2 norm

$$\sqrt{\delta^{(K)}} = \left\| \rho^{(K)} - \rho_{\text{Haar}}^{(K)} \right\|_2 / \left\| \rho_{\text{Haar}}^{(K)} \right\|_2. \quad (\text{A3})$$

At the end, we present the theoretical result for the dynamics of higher-order frame potentials in HDT,

**Lemma 4** *The typical  $K$ -th frame potential  $\mathcal{F}^{(K)}(t)$  ( $K > 1$ ) of the projected ensemble  $\mathcal{E}_t$  at step  $t$  in the holographic deep thermalization has an asymptotic lower bound ( $d_A \gg 1$ )*

$$\mathcal{F}^{(K)}(t) \gtrsim \left( \frac{d_A^2 d_B}{d_A^2 d_B^2 - 1} \right)^t \simeq \left( \frac{1}{d_B} \right)^t. \quad (\text{A4})$$

The proof can be found in C. One can immediately realize that the higher-order frame potentials share the same decay rate as the one in the first-order measure (see Theorem 1).

### 2. Details of experiments

We validate the *projected ensemble* of HDT through experiments conducted on IBM Quantum devices [31]. Our implementation utilizes the mid-circuit measurement and reset.

In Fig. 2a, we implement the hardware efficient ansatz (HEA) [32] with  $L = 4$  layers on a system of  $N_A = 2, N_B = 2$  qubits to generate sufficiently random and complex unitaries at each time step of HDT. To evaluate the first-order frame potential, we equivalently evaluate the purity of the average state of the *projected ensemble* on the data system via

$$\text{tr}\left((\rho^{(1)})^2\right) = \frac{1}{d} \sum_{P \in \mathcal{P}_{N_A}} \text{tr}\left(\rho^{(1)} P\right)^2, \quad (\text{A5})$$

where  $\mathcal{P}_{N_A}$  is the Pauli group on  $N_A$  qubits omitting phases, and  $\rho^{(1)}$  is the first-order moment operator defined in Eq. (A1). Each blue dot in Fig. 2a represents an average over 100 sets of randomly initialized HEA parameters, implemented on IBM Quantum Sherbrooke. For each Pauli expectation in Eq. (A5), we take 4096 measurement shots for an accurate estimation. For future extension to large data systems, the classical shadow [8] provides an alternative efficient method to estimate purity.

In Fig. 2b-d, the HEA is employed again to compute the PoP of *projected ensembles* with  $L = N_A + N_B$  layers of circuits in each step. Unlike the frame potential experiment, a single set of circuit gate parameters is randomly chosen and kept fixed across repetitions. For each experiment,  $10^5$  measurement shots are taken to gather a sufficient number of measurement strings from the joint system. The experiments are repeated 10 times on IBM Quantum Brisbane

to obtain the average PoP at different time steps in various systems. Noiseless and noisy simulations are performed using the same setup, with ideal and noisy circuit models provided by IBM Quantum Qiskit. For a  $N_A = 2$  qubit system with dimension  $d_A = 4$ , we choose  $N_B = 2$  ancilla qubits and implement six steps of HDT, each step with a circuit depth of 4. For a  $N_A = 4$  qubit system ( $d_A = 16$ ), we still choose  $N_B = 2$  ancilla qubits and implement six steps of HDT, each step with a circuit depth of 6. We also extend the experiment to  $N_A = 5$  qubits ( $d_A = 32$ ) with  $N_B = 3$  ancilla and three steps, each step with a circuit depth of 8.

In Fig. 3d, we follow the same design as in Fig. 2a on a system of  $N_A = 2$  data qubits but with different  $N_B$  ancilla qubits and time steps  $T$ . The circuit depth is chosen to be  $L = 2 + N_B$  layers. Each blue bar is averaged over 10 sets of randomly initialized HEA circuits implemented on IBM Quantum Brisbane.

In the end, we list some of the median calibration data of IBM Quantum Sherbrooke and Brisbane in Table I.

Error	Sherbrooke	Brisbane
2-qubit Gate Error	$7.536 \times 10^{-3}$	$8.006 \times 10^{-3}$
Readout Error	0.0133	0.0154
$T_1$	272.47 $\mu$ s	228.99 $\mu$ s
$T_2$	175.87 $\mu$ s	143.04 $\mu$ s

Table I. Median calibration data of the IBM devices.

### 3. Quantum machine learning enhancement

The task of random quantum state generation can be considered as a quantum transport problem from a Dirac- $\delta$  distributed ensemble of a single initial state towards the Haar ensemble of states. In this regard, we can further enhance HDT via generative quantum machine learning (QML) [33]. As shown in Fig. 5a, we parameterize the unitary at time step  $t$  as  $U(\theta_t)$  and optimize the parameters  $\{\theta_t\}_{t=1}^T$  to obtain the best approximate Haar random ensemble at the output.

Towards this goal, we consider a divide-and-conquer strategy of only training the unitary  $U(\theta_t)$  in the  $t$ -th step, via minimizing a loss function  $\mathcal{L}_t(\mathcal{E}_t)$  on the state ensemble  $\mathcal{E}_t$ . While a greedy strategy may hope for  $\mathcal{E}_t$  to be close to Haar random ensemble  $\mathcal{E}_{\text{Haar}}$  at each training step, we take a less greedy cost function  $\mathcal{L}_t(\mathcal{E}_t) = (1 - q_t)D(\mathcal{E}_t, |\psi_0\rangle) + q_tD(\mathcal{E}_t, \mathcal{E}_{\text{Haar}})$  as an interpolation of ‘distances’ to the initial single-state  $|\psi_0\rangle$  and Haar ensemble, with a monotonically increasing scheduling function  $q_t \in [0, 1]$ . Here  $D(\cdot, \cdot)$  characterize the ‘distance’ between two ensembles (see Appendix G). To enable efficient evaluation of the loss function on actual quantum devices, we consider the simplest choice of ‘distance’  $D(\cdot, \cdot)$ , the super-fidelity between the average state  $\rho_t = \mathbb{E}_{\phi \sim \mathcal{E}_t} |\phi\rangle\langle\phi|$  of the ensembles—only keeping track of the first-moment information. We expect that the final generated state ensemble  $\mathcal{E}_T$  is still able to capture some of the higher-moment properties of true Haar ensemble through a large enough number of steps  $T$  thus sufficient randomness from measurements.

We numerically simulate the training of the QML-enhanced HDT with  $T = 32$  and  $N_B = 1$  and the results are presented in Fig. 5bc, where QML-enhanced frame potential (blue dots) lies very close to the exact Haar value (black dashed), up to deviations caused by finite samples indicated by the finite-sampling Haar results (gray dots). Constant advantage over the untrained HDT is obtained via the QML enhancement. Details of the quantum circuit ansatz and training are provided in Appendix G.

### 4. Numerical simulation details

We numerically simulate the HDT without/with QML enhancement utilizing `TensorCircuit` [34].

In Fig. 2a and Fig. 3ab, each dot of numerical simulation is an average over 20 random Haar unitary realizations, where each ensemble consists of  $5 \times 10^4$  samples.

In Fig. 4b, the average mutual information and corresponding Rényi lower bound for both conventional deep thermalization and HDT are evaluated exactly over all possible measurement results given  $t \leq 8$ , meanwhile for  $t > 8$ , we take Monte-Carlo sampling over  $2 \times 10^4$  measurement results. We further average over 50 randomly sampled Haar unitary realizations.

In Fig. 5, for holographic deep thermalization with random unitary implementation, we average over 50 Haar unitaries realizations with ensemble of  $5 \times 10^4$  samples. For QML-enhanced holographic deep thermalization, we average over 20 post-measurement ensembles, each of which includes  $5 \times 10^4$  samples. The empirical  $\mathcal{F}_{\text{Haar}}^{(K)}$  is averaged over 50 ensembles of  $5 \times 10^4$  Haar random states.



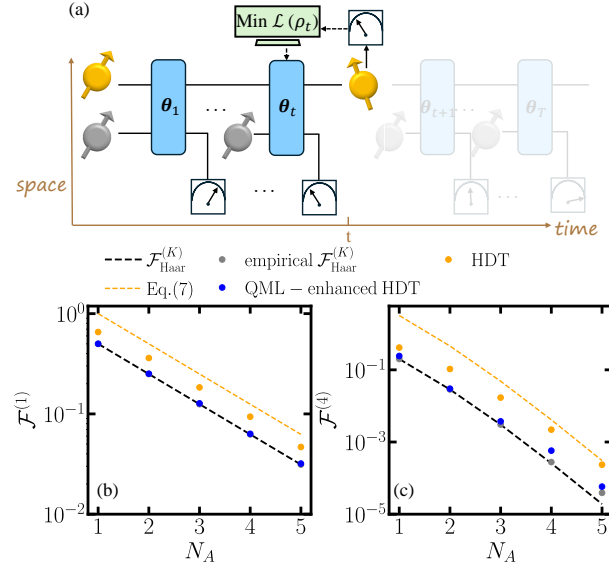


Figure 5. QML-enhanced HDT. In (a), we show the conceptual plot of the training process. In (b) and (c), we show the frame potential for  $K = 1$  and  $K = 4$  of output state ensemble. Orange dots represent converged frame potential in HDT with random unitary implementation. Orange dashed line is the theoretical prediction in Eq. (3). Blue dots are frame potential of output state ensemble from QML-enhanced HDT. Black dashed line and gray dots show the exact and empirical of Haar ensemble frame potential.

## Appendix B: Preliminary

To quantify the approximation of an arbitrary state ensemble  $\mathcal{E}$  to Haar ensemble ( $K$ -design), we consider the (normalized)  $p$ -order moment distance and the relative deviation of frame potential as [14]

$$\Delta_{\mathcal{E},p}^{(K)} = \frac{\left\| \rho_{\mathcal{E}}^{(K)} - \rho_{\text{Haar}}^{(K)} \right\|_p}{\left\| \rho_{\text{Haar}}^{(K)} \right\|_p}, \quad (\text{B1})$$

$$\delta_{\mathcal{E}}^{(K)} = \frac{\mathcal{F}_{\mathcal{E}}^{(K)}}{\mathcal{F}_{\text{Haar}}^{(K)}} - 1, \quad (\text{B2})$$

where  $\|\cdot\|_p$  is the  $p$ -Schatten norm and  $\rho_{\mathcal{E}}^{(K)}$  is defined in Eq. (A1) of the main text. Commonly used order of norms include  $p = 1$  (trace norm),  $p = 2$  (Frobenius norm) and  $p = \infty$  (operator norm). Note that  $\left\| \rho_{\text{Haar}}^{(K)} \right\|_1 = 1$ , then

$$\Delta_{\mathcal{E},1}^{(K)} = \left\| \rho_{\mathcal{E}}^{(K)} - \rho_{\text{Haar}}^{(K)} \right\|_1 = 2D_{\text{tr}} \left( \rho_{\mathcal{E}}^{(K)}, \rho_{\text{Haar}}^{(K)} \right), \quad (\text{B3})$$

which is equivalent to trace distance between  $K$ -th-moment of  $\mathcal{E}$  and Haar, widely explored in Refs. [12, 13]. We can also show that for  $p = 2$ , it is equivalent to the frame potential as [14]

$$\Delta_{\mathcal{E},2}^{(K)} = \frac{\left\| \rho_{\mathcal{E}}^{(K)} - \rho_{\text{Haar}}^{(K)} \right\|_2}{\left\| \rho_{\text{Haar}}^{(K)} \right\|_2} \quad (\text{B4})$$

$$= \frac{\text{tr} \left[ \left( \rho_{\mathcal{E}}^{(K)} - \rho_{\text{Haar}}^{(K)} \right)^2 \right]^{1/2}}{\text{tr} \left[ \left( \rho_{\text{Haar}}^{(K)} \right)^2 \right]^{1/2}} \quad (\text{B5})$$

$$= \left( \frac{\mathcal{F}_{\mathcal{E}}^{(K)} - \mathcal{F}_{\text{Haar}}^{(K)}}{\mathcal{F}_{\text{Haar}}^{(K)}} \right)^{1/2} = \sqrt{\delta_{\mathcal{E}}^{(K)}}, \quad (\text{B6})$$

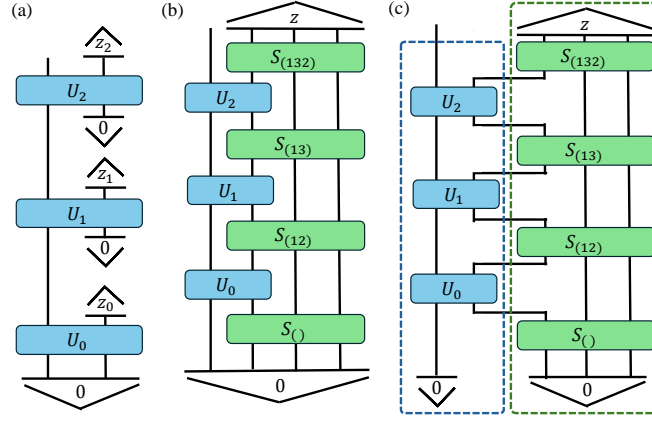


Figure 6. (a) Circuit diagram of holographic deep thermalization. Data and bath subsystems are both initialized in  $|0\rangle$ , evolved by a chaotic Hamiltonian, and followed by projective measurements and reset on bath. In (b), we show the equivalent circuit diagram by postponing projective measurements to the end. Here  $S_\pi$  represents the permutation operator of  $\pi$ , e.g.  $S_{(12)}$  represents the swap between  $B_1, B_2$ . In (c), we split the circuit in (b) into two parts, separated by a “temporal” cut. A state  $|\phi_z\rangle$  on “temporal” cut produced by the map (green box) is taken as the input into the linear map (blue box) in the left, and outputs the post-measurement on subsystem  $A$ . Here we plot the system of three steps.

where we utilize  $\text{tr}(\rho_{\mathcal{E}}^{(K)} \rho_{\text{Haar}}^{(K)}) = \mathcal{F}_{\text{Haar}}^{(K)}$  in the third line. The norm with  $p = 1$  can also be bounded by  $p = 2$  norm with norm inequalities, therefore we mainly focus on the frame potential in the main text.

### Appendix C: Dynamics of frame potential in holographic deep thermalization

In this section, we derive the frame potential dynamics in the holographic deep thermalization. Without losing generality, we model each unitary evolution  $U_t$  as a random unitary sampled from the Haar group  $\mathcal{U}_{\text{Haar}}$ . At step  $t$  in the holographic deep thermalization model, the input involves two parts, the data and bath side with qubits  $N_A, N_B$  thus dimension  $d_A = 2^{N_A}, d_B = 2^{N_B}$ . The derivation follows the notation conventions in Ref. [35]. Before doing the detailed calculation, we would like to clarify we are calculating the frame potential—purity of  $K$ -th moment state  $\rho^{(K)}$ —and then take the average; Taking an average first over the state will not lead to typical case results of a fixed sequence of unitaries. Indeed, the average state becomes fully mixed even just with a single step.

For the holographic deep thermalization shown in Fig. 6a, the joint system of  $A, B$  is initialized at  $|0\rangle$ , and in step  $t$ , we apply a Haar random unitary  $U_{t-1}$  on the joint system, followed by projective measurement and reset on  $B$ . Equivalently, we can postpone all mid-circuit measurements to the end of the circuit evolution while expanding the bath system to  $B \rightarrow B_1, \dots, B_T$  shown in Fig. 6b. Here the  $S_\pi$  represents the permutation operation of  $\pi$  on the expanded bath. We can further split the circuit into two parts by a “temporal cut”  $C$  (see Fig. 6c), which enables us an analytical analysis on the dynamics through the replica trick. The right block (enclosed by green dashed box) provides the  $d_B^{2T}$ -dimensional state  $|\phi_z\rangle = \otimes_{t=0}^{T-1} |0\rangle |z_t\rangle$  on the “time bond”. The left block (enclosed by blue dashed box), can thus be regarded as a linear map  $E$  applied on the “time bond” space and map it to subsystem  $A$ . The linear map can be explicitly written as

$$E_{a,c} = \sum_{\alpha} \prod_{t=0}^{T-1} \langle \alpha_{t+1}, c_{2t+1} | U_t | \alpha_t, c_{2t} \rangle \delta_{\alpha_0, 0} \delta_{\alpha_T, a} | a \rangle \langle c_{2T-1} | \dots \langle c_0 |, \quad (\text{C1})$$

where  $a$  is the index on subsystem  $A$  and  $c$  is the index on the temporal cut. The *projected ensemble* on  $A$  at step  $T$  can then be written as

$$\mathcal{E}(T) = \{p_z = \langle \phi_z | E^\dagger E | \psi_z \rangle, |\psi_z\rangle = E |\phi_z\rangle / \sqrt{p_z}, z = 0, \dots, d_B^T - 1\}. \quad (\text{C2})$$

We derive the dynamics of frame potentials for  $\mathcal{E}(T)$  in the following.

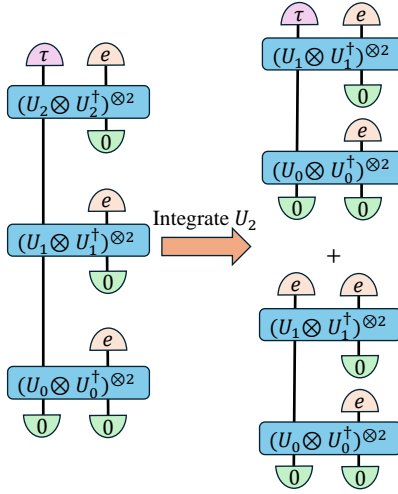


Figure 7. Tensor network representation of first-order frame potential. In the left we plot the case involving three steps. Each semi-circle represents the operator over two replicas. By integrating out the unitary  $U_2$  over Haar unitary group, we reach the two terms in the right (omitting coefficients). The boundary condition is either the same as the one before integration or trivial to be invariant under unitary evolution.

### 1. First order frame potential dynamics

For  $K = 1$ , the first moment of ensemble  $\mathcal{E}(T)$  is

$$\rho_A^{(1)}(T) = \sum_z p_z |\psi_z\rangle\langle\psi_z| = \sum_z E |\phi_z\rangle\langle\phi_z| E^\dagger. \quad (\text{C3})$$

Note that

$$\sum_z |\phi_z\rangle\langle\phi_z| = \sum_z |z_{T-1}\rangle\langle z_{T-1}| \otimes |0\rangle\langle 0| \cdots |z_0\rangle\langle z_0| \otimes |0\rangle\langle 0| = (\mathbf{I} \otimes |0\rangle\langle 0|)^{\otimes T}, \quad (\text{C4})$$

where  $\mathbf{I}$  is the identity operation of dimension  $d_B$ . Therefore, the first moment becomes

$$\rho_A^{(1)}(T) = \sum_z E |\phi_z\rangle\langle\phi_z| E^\dagger \quad (\text{C5})$$

$$= E (\mathbf{I} \otimes |0\rangle\langle 0|)^{\otimes T} E^\dagger \quad (\text{C6})$$

$$= \sum_{\alpha, \alpha'} \sum_{\mathbf{c}} \prod_{t=0}^{T-1} \langle \alpha_{t+1}, c_{2t+1} | U_t | \alpha_t, 0 \rangle \langle \alpha'_t, 0 | U_t^\dagger | \alpha'_{t+1}, c_{2t+1} \rangle \delta_{\alpha_0, 0} \delta_{\alpha'_0, 0} \delta_{\alpha_T, a} \delta_{\alpha'_T, a'} |a\rangle\langle a'| \quad (\text{C7})$$

$$= \sum_{\alpha, \alpha'} \prod_{t=0}^{T-1} \text{tr} \left( U_t (|\alpha_t\rangle\langle\alpha'_t|_A \otimes |0\rangle\langle 0|) U_t^\dagger |\alpha'_{t+1}\rangle\langle\alpha_{t+1}| \right) \delta_{\alpha_0, 0} \delta_{\alpha'_0, 0} \delta_{\alpha_T, a} \delta_{\alpha'_T, a'} |a\rangle\langle a'|. \quad (\text{C8})$$

From Eq. (1) of the main text, the first-order frame potential is the purity of first moment as

$$\mathcal{F}^{(1)}(T) = \text{tr} \left( \rho_A^{(1)}(T)^2 \right) \quad (\text{C9})$$

$$\begin{aligned} &= \sum_{a, a'} \sum_{\alpha, \alpha', \beta, \beta'} \prod_{t=0}^{T-1} \text{tr} \left( U_t (|\alpha_t\rangle\langle\alpha'_t|_A \otimes |0\rangle\langle 0|) U_t^\dagger |\alpha'_{t+1}\rangle\langle\alpha_{t+1}| \right) \text{tr} \left( U_t (|\beta_t\rangle\langle\beta'_t|_A \otimes |0\rangle\langle 0|) U_t^\dagger |\beta'_{t+1}\rangle\langle\beta_{t+1}| \right) \\ &\quad \times \delta_{\alpha_0, 0} \delta_{\alpha'_0, 0} \delta_{\alpha_T, a} \delta_{\alpha'_T, a'} \delta_{\beta_0, 0} \delta_{\beta'_0, 0} \delta_{\beta_T, a'} \delta_{\beta'_T, a}. \end{aligned} \quad (\text{C10})$$

$$\begin{aligned} &= \sum_{a, a'} \sum_{\alpha, \alpha', \beta, \beta'} \prod_{t=0}^{T-1} \text{tr} \left( U_t^{\otimes 2} (|\alpha_t, \beta_t\rangle\langle\alpha'_t, \beta'_t|_A \otimes |0, 0\rangle\langle 0, 0|) U_t^{\dagger \otimes 2} |\alpha'_{t+1}, \beta'_{t+1}\rangle\langle\alpha_{t+1}, \beta_{t+1}| \right) \\ &\quad \times \delta_{\alpha_0, 0} \delta_{\alpha'_0, 0} \delta_{\alpha_T, a} \delta_{\alpha'_T, a'} \delta_{\beta_0, 0} \delta_{\beta'_0, 0} \delta_{\beta_T, a'} \delta_{\beta'_T, a}, \end{aligned} \quad (\text{C11})$$

which can be represented by a tensor diagram as in the left panel of Fig. 7, where the boundary condition is the transposition  $|\tau\rangle$  over two replicas in  $A$  and identity operator  $|e\rangle$ . Here we denote  $|A\rangle = \sum_{i,j} A_{i,j} |i\rangle |j\rangle$  as the vectorized operator following the convention in Ref. [35], and  $(A|B) = \text{tr}(A^\dagger B)$ . We can now perform the Haar unitary ensemble average from  $U_{T-1}$  backwards to  $U_0$ . The unitary twirling channel over Haar random unitary [2] is

$$\mathbb{E}_{V \sim \mathcal{U}_{\text{Haar}}(d)} [V^{\otimes 2} \otimes V^{\dagger \otimes 2}] = \frac{1}{d^2 - 1} \left( |e\rangle\langle e| - \frac{1}{d} |e\rangle\langle \tau| + |\tau\rangle\langle \tau| - \frac{1}{d} |\tau\rangle\langle e| \right). \quad (\text{C12})$$

Therefore the ensemble average over  $U_{T-1}$  on boundary condition  $|\tau\rangle_A |e\rangle_B$  becomes

$$\mathbb{E}_{U_{T-1} \sim \mathcal{U}_{\text{Haar}}} \left[ U_{T-1}^{\otimes 2} \otimes U_{T-1}^{\dagger \otimes 2} \right] |\tau\rangle_A |e\rangle_B = \frac{1}{d_A^2 d_B^2 - 1} \left( |e\rangle\langle e| - \frac{1}{d} |e\rangle\langle \tau| + |\tau\rangle\langle \tau| - \frac{1}{d} |\tau\rangle\langle e| \right) |\tau\rangle_A |e\rangle_B \quad (\text{C13})$$

$$= \frac{1}{d_A^2 d_B^2 - 1} \left( \left[ |e\rangle\langle \tau|_A d_B^2 - \frac{d_A^2 (\tau|e)_B}{d} \right] |e\rangle_A |e\rangle_B + \left[ d_A^2 (\tau|e)_B - \frac{(e|\tau)_A d_B^2}{d} \right] |\tau\rangle_A |\tau\rangle_B \right) \quad (\text{C14})$$

$$= \frac{d_B(d_A^2 - 1)}{d_A^2 d_B^2 - 1} |\tau\rangle_A |\tau\rangle_B + \frac{d_A(d_B^2 - 1)}{d_A^2 d_B^2 - 1} |e\rangle_A |e\rangle_B. \quad (\text{C15})$$

We then apply  $|e\rangle\langle 0|_B$  on subsystem  $B$  and have

$$|e\rangle\langle 0|_B \mathbb{E}_{U_{T-1} \sim \mathcal{U}_{\text{Haar}}} \left[ U_{T-1}^{\otimes 2} \otimes U_{T-1}^{\dagger \otimes 2} \right] |\tau\rangle_A |e\rangle_B = \frac{d_B(d_A^2 - 1)}{d_A^2 d_B^2 - 1} (0|\tau\rangle_B |\tau\rangle_A |e\rangle_B) + \frac{d_A(d_B^2 - 1)}{d_A^2 d_B^2 - 1} (0|e\rangle_B |e\rangle_A |e\rangle_B) \quad (\text{C16})$$

$$= \frac{d_B(d_A^2 - 1)}{d_A^2 d_B^2 - 1} |\tau\rangle_A |e\rangle_B + \frac{d_A(d_B^2 - 1)}{d_A^2 d_B^2 - 1} |e\rangle_A |e\rangle_B \quad (\text{C17})$$

where we utilize  $(0|\hat{\sigma})_B = 1$  for any permutation  $\sigma$ . The first and second part correspond to the right panel of Fig. 7. We see that the first part is the same boundary condition as in step  $T$ , while the second part remains invariant in the backward process. We are now ready to derive the recurrent equation for ensemble average frame potential as

$$\mathbb{E}_{\text{Haar}} \left[ \mathcal{F}^{(1)}(T) \right] = \frac{d_B(d_A^2 - 1)}{d_A^2 d_B^2 - 1} \mathbb{E}_{\text{Haar}} \left[ \mathcal{F}^{(1)}(T-1) \right] + \frac{d_A(d_B^2 - 1)}{d_A^2 d_B^2 - 1}, \quad (\text{C18})$$

with initial condition  $\mathbb{E}_{\text{Haar}} \left[ \mathcal{F}^{(1)}(0) \right] = 1$ . The recurrent equation can be analytically solved as

$$\mathbb{E}_{\text{Haar}} \left[ \mathcal{F}^{(1)}(t) \right] = \frac{(d_A - 1)(d_A d_B - 1)}{d_A^2 d_B + 1} \left( \frac{(d_A^2 - 1) d_B}{d_A^2 d_B^2 - 1} \right)^t + \frac{d_A(d_B + 1)}{d_A^2 d_B + 1} \mathcal{F}_{\text{Haar}}^{(1)}, \quad (\text{C19})$$

where  $\mathcal{F}_{\text{H}}^{(1)} = 1/d_A$  is the first-order frame potential of Haar ensemble. In the thermodynamic limit of large number of data qubits  $d_A \rightarrow \infty$ , it can be reduced to

$$\mathbb{E}_{\mathcal{U}_{\text{H}}} \left[ \mathcal{F}^{(1)}(t) \right] = d_B^{-t} + \left( 1 + \frac{1}{d_B} \right) \mathcal{F}_{\text{H}}^{(1)}. \quad (\text{C20})$$

We also notice that it reproduces the known result in Ref. [13] by taking  $t = 1$ . In the main text, we adopt the Haar ensemble averaged quantities to represent the typical case and omitted the notation of  $\mathbb{E}_{\mathcal{U}_{\text{H}}}$ .

## 2. Higher order frame potential dynamics

In this part, we derive a phenomenological equation of the dynamics for higher-order frame potential. Following the ensemble (Eq. (C2)) at step  $T$ , the  $K$ -th moment is

$$\rho_A^{(K)}(T) = \sum_z p_z |\psi_z\rangle\langle\psi_z|^{\otimes K} \quad (\text{C21})$$

$$= \sum_z \langle\phi_z|E^\dagger E|\phi_z\rangle^{1-K} (E|\phi_z\rangle\langle\phi_z|E^\dagger)^{\otimes K}. \quad (\text{C22})$$

We utilize the replica-trick [36] as in other studies. We first define a psuedo moment

$$\rho_A^{(m,K)}(T) = \sum_z \langle \phi_z | E^\dagger E | \phi_z \rangle^m (E | \phi_z \rangle \langle \phi_z | E^\dagger)^{\otimes K} \quad (\text{C23})$$

$$= \text{tr}_{A_{1:m}} \left( \sum_z (E | \phi_z \rangle \langle \phi_z | E^\dagger)^{\otimes m+K} \right) \quad (\text{C24})$$

and take the limit  $m \rightarrow 1 - K$  at the end. In the last line we trace out the first  $m$  replicas. For convenience, we define  $r = m + K$ . Note that

$$\sum_z |\phi_z \rangle \langle \phi_z|^{\otimes r} = \sum_z \left( \otimes_{t=0}^{T-1} |z_t \rangle \langle z_t| \otimes |0 \rangle \langle 0| \right)^{\otimes r} \quad (\text{C25})$$

$$= \sum_z \otimes_{t=0}^{T-1} |z_t^r \rangle \langle z_t^r| \otimes |0^r \rangle \langle 0^r| \quad (\text{C26})$$

$$= \otimes_{t=0}^{T-1} \left( \sum_{z_t} |z_t^r \rangle \langle z_t^r| \otimes |0^r \rangle \langle 0^r| \right) \quad (\text{C27})$$

$$= (D_r \otimes |0^r \rangle \langle 0^r|)^{\otimes T}, \quad (\text{C28})$$

where for simplicity of notation, we denote  $|b^r \rangle = |b^{\otimes r} \rangle$ . Here  $D_r$  is the projector onto the space of  $r$  replicas. The pseudo moment operator then becomes

$$\rho_A^{(m,K)}(T) = \text{tr}_{A_{1:m}} (E^{\otimes r} (D_r \otimes |0^r \rangle \langle 0^r|)^{\otimes T} E^{\dagger \otimes r}), \quad (\text{C29})$$

and the psuedo frame potential is

$$\mathcal{F}^{(m,K)}(T) = \text{tr} \left( \rho_A^{(m,K)}(T)^2 \right) \quad (\text{C30})$$

$$= \text{tr} \left[ \text{tr}_{A_{1:m}} (E^{\otimes r} (D_r \otimes |0^r \rangle \langle 0^r|)^{\otimes T} E^{\dagger \otimes r})^2 \right] \quad (\text{C31})$$

$$= \text{tr} \left( E^{\otimes 2r} (D_r^{\otimes 2} \otimes |0^{2r} \rangle \langle 0^{2r}|)^{\otimes T} E^{\dagger \otimes 2r} \tau \right), \quad (\text{C32})$$

where  $\tau$  is a transposition operator nontrivially applied on the last  $K$  copies within first  $r$  and second  $r$  replicas, thus the expression above can also be written as in a tensor diagram similar to Fig. 7, where the boundary condition becomes  $D_r^{\otimes 2}$  on subsystem  $B$ , and transposition  $\tau$  over  $2K$  replicas only on subsystem  $A$ . For unitary twirling over  $r$  replicas, we have

$$\mathbb{E} \left[ (U \otimes U^\dagger)^{\otimes 2r} \right] = \sum_{\sigma, \pi \in S_{2r}} \text{Wg}(\sigma^{-1}\pi, 2r) |\hat{\sigma}\rangle \langle \hat{\pi}| \simeq \text{Wg}(e, 2r) \sum_{\sigma \in S_{2r}} |\hat{\sigma}\rangle \langle \hat{\sigma}|, \quad (\text{C33})$$

where  $S_{2r}$  is the permutation group over  $2r$  replicas, and  $\hat{\pi}$  is the operator representation of permutation  $\pi$ .  $\text{Wg}(\sigma^{-1}\pi, 2r)$  is the Weingarten coefficient defined to be  $\text{Wg}(\sigma^{-1}\pi, 2r) = \left( d^{|\sigma^{-1}\pi|} \right)^{-1}$  where  $|\sigma^{-1}\pi|$  denotes the number of cycles in the permutation  $\sigma^{-1}\pi$ . In the large dimension limit  $d \gg 1$ , we can only keep the leading order coefficient with  $\sigma = \pi$ , leading to the approximation. Following the same backward formalism, we start from the end as

$$|D_r^{\otimes 2}\rangle \langle 0^{2r}|_B \mathbb{E} \left[ (U \otimes U^\dagger)^{\otimes 2r} \right] |\tau\rangle_A |D_r^{\otimes 2}\rangle_B \quad (\text{C34})$$

$$\simeq \text{Wg}(e, 2r) |D_r^{\otimes 2}\rangle \langle 0^{2r}|_B \sum_{\sigma} (\sigma|\tau\rangle_A \langle \sigma|D_r^{\otimes 2}\rangle_B |\sigma\rangle_A |\sigma\rangle_B) \quad (\text{C35})$$

$$= \text{Wg}(e, 2r) (\tau|\tau\rangle_A \langle \tau|D_r^{\otimes 2}\rangle_B \langle 0^{2r}|\tau\rangle_B |\tau\rangle_A |D_r^{\otimes 2}\rangle_B + \text{Wg}(e, 2r) \sum_{\sigma \neq \tau} (\sigma|\tau\rangle_A \langle \sigma|D_r^{\otimes 2}\rangle_B \langle 0^{2r}|\sigma\rangle_B |\sigma\rangle_A |D_r^{\otimes 2}\rangle_B) \quad (\text{C36})$$

$$= \text{Wg}(e, 2r) d_A^{2r} (\tau|D_r^{\otimes 2}\rangle_B |\tau\rangle_A |D_r^{\otimes 2}\rangle_B + \text{Wg}(e, 2r) \sum_{\sigma \neq \tau} (\sigma|\tau\rangle_A \langle \sigma|D_r^{\otimes 2}\rangle_B |\sigma\rangle_A |D_r^{\otimes 2}\rangle_B). \quad (\text{C37})$$

For an arbitrary  $\sigma \in S_{2r}$ , we have

$$(\sigma|D_2^{\otimes 2})_B = \text{tr}(\sigma^\dagger D_2^{\otimes 2}) \quad (\text{C38})$$

$$= \sum_{z, z'} \langle z^r z'^r | \sigma^\dagger | z^r z'^r \rangle \quad (\text{C39})$$

$$= \sum_z \langle z^{2r} | \sigma^\dagger | z^{2r} \rangle + \sum_{z \neq z'} \langle z^r z'^r | \sigma^\dagger | z^r z'^r \rangle \quad (\text{C40})$$

$$= d_B + d_B(d_B - 1)\delta_{\sigma^\dagger, \sigma_1 \sigma_2}, \quad \sigma_1, \sigma_2 \in S_r. \quad (\text{C41})$$

Then the first part in Eq. (C37) is

$$\text{Wg}(e, 2r) d_A^{2r} (\tau|D_r^{\otimes 2})_B |\tau\rangle_A |D_r^{\otimes 2})_B = \text{Wg}(e, 2r) d_A^{2r} d_B |\tau\rangle_A |D_r^{\otimes 2})_B, \quad (\text{C42})$$

which recovers the boundary condition before the backward process. For the second term, the coefficients satisfy  $(\sigma|\tau)_A = \text{tr}(\sigma^\dagger \tau)_A = d^{|\sigma^\dagger \tau|} > 0$  and  $(\sigma|D_r^{\otimes 2}) = \text{tr}(\sigma^\dagger \sum_{z, z'} |z^r\rangle\langle z^r| \otimes |z'^r\rangle\langle z'^r|) \geq 0$ . By discarding any potential existing time-dependent contribution in the second term, we have

$$\mathbb{E}_{\text{Haar}} [\mathcal{F}^{(m, K)}(T)] \geq \frac{d_A^2 d_B}{d_A^2 d_B^2 - 1} \mathbb{E}_{\text{Haar}} [\mathcal{F}^{(m, K)}(T - 1)], \quad (\text{C43})$$

which immediately brings us the lower bound on the pseudo frame potential as

$$\mathbb{E}_{\text{Haar}} [\mathcal{F}^{(m, K)}(T)] \geq \left( \frac{d_A^2 d_B}{d_A^2 d_B^2 - 1} \right)^T \mathbb{E}_{\text{Haar}} [\mathcal{F}^{(m, K)}(0)] = \left( \frac{d_A^2 d_B}{d_A^2 d_B^2 - 1} \right)^T. \quad (\text{C44})$$

Here we have used the initial condition  $\mathbb{E}_{\text{Haar}} [\mathcal{F}^{(m, K)}(0)] = 1$ . Lemma 4 of the main text is thus proved by taking the limit of  $m \rightarrow 1 - K$ .

We next takes an approximation to precisely handle the second term. We consider a subset of permutations  $\sigma \in \mathcal{S}$  such that

$$|D_r^{\otimes 2})(0^{2r}| \mathbb{E} [(U \otimes U^\dagger)^{\otimes 2r}] |\sigma\rangle_A |D_r^{\otimes 2})_B \propto |\sigma\rangle_A |D_r^{\otimes 2})_B \quad (\text{C45})$$

in the leading order. These permutations will remain invariant through the following unitary twirlings which contribute to the time-invariant term in the recurrent equation, modeled as a constant  $q$ . Therefore, we have

$$\mathbb{E}_{\text{Haar}} [\mathcal{F}^{(m, K)}(T)] \geq \text{Wg}(e, 2) \left( d_A^2 d_B \mathbb{E}_{\text{Haar}} [\mathcal{F}^{(m, K)}(T - 1)] + q \right) \quad (\text{C46})$$

$$= \frac{1}{d_A^2 d_B^2 - 1} \left( d_A^2 d_B \mathbb{E}_{\text{Haar}} [\mathcal{F}^{(m, K)}(T - 1)] + q \right) \quad (\text{C47})$$

$$= \frac{d_A^2 d_B}{d_A^2 d_B^2 - 1} \mathbb{E}_{\text{Haar}} [\mathcal{F}^{(m, K)}(T - 1)] + \frac{q}{d_A^2 d_B^2 - 1}, \quad (\text{C48})$$

where  $q$  is defined as

$$q = \sum_{\sigma \in \mathcal{S}, \sigma \neq \tau} (\sigma|\tau)_A (\sigma|D_r^{\otimes 2})_B, \quad (\text{C49})$$

which is a positive constant. The pseudo frame potential can thus be solved as

$$\mathbb{E}_{\text{Haar}} [\mathcal{F}^{(m, K)}(t)] \geq (1 - q) \left( \frac{d_A^2 d_B}{d_A^2 d_B^2 - 1} \right)^t + q. \quad (\text{C50})$$

where we redefine  $q \rightarrow q/(d_A^2(d_B - 1)d_B - 1)$  for simplicity. In the thermodynamic limit  $d_A \rightarrow \infty$ , it can be further reduced to

$$\mathbb{E}_{\text{Haar}} [\mathcal{F}^{(m, K)}(t)] \geq (1 - q) \left( \frac{1}{d_B} \right)^t + q, \quad (\text{C51})$$

where  $q = (1 + (2^K - 1)/d_B) \mathcal{F}_{\text{Haar}}^{(K)}$  is found empirically as detailed in F.

### Appendix D: Average mutual information in deep thermalization

In this section, we derive the asymptotic lower bound for the measurement-averaged mutual information in regular deep thermalization. We begin with connecting the average mutual information to average purity as follows.

$$\mathbb{E}_{\mathbf{z}} I(R : A_{\text{out}}|\mathbf{z}) \equiv \mathbb{E}_{\mathbf{z}} [S(R|\mathbf{z}) + S(A_{\text{out}}|\mathbf{z}) - S(RA_{\text{out}}|\mathbf{z})] \quad (\text{D1})$$

$$= \mathbb{E}_{\mathbf{z}} 2S(A_{\text{out}}|\mathbf{z}) \quad (\text{D2})$$

$$\geq \mathbb{E}_{\mathbf{z}} 2S_2(A_{\text{out}}|\mathbf{z}) = -2\mathbb{E}_{\mathbf{z}} \log_2 \left( \text{tr} \left( \rho_{A_{\text{out}}|\mathbf{z}}^2 \right) \right) \quad (\text{D3})$$

$$\geq -2\log_2 \left( \mathbb{E}_{\mathbf{z}} \text{tr} \left( \rho_{A_{\text{out}}|\mathbf{z}}^2 \right) \right), \quad (\text{D4})$$

where in Eq. (D1)  $S(R|\mathbf{z})$  is the von-Neumann entanglement entropy of reduced state  $\rho_{R|\mathbf{z}} = \text{tr}_{A_{\text{out}}}(|\psi_{\mathbf{z}}\rangle\langle\psi_{\mathbf{z}}|_{RA_{\text{out}}})$  and so as others. Eq. (D2) comes from the fact that the conditional state on  $RA_{\text{out}}|\psi_{\mathbf{z}}\rangle\langle\psi_{\mathbf{z}}|$  is a pure state. We utilize the monotonicity in Rényi entropy to obtain Ineq. (D3). We obtain the last inequality of Eq. (D4) utilizing the concavity of logarithmic function. Due to the same reason, we can further lower bound the Haar-averaged of Eq. (D4) as

$$\mathbb{E}_{\text{Haar}} \mathbb{E}_{\mathbf{z}} I(R : A_{\text{out}}|\mathbf{z}) \geq -2\mathbb{E}_{\text{Haar}} \log_2 \left( \mathbb{E}_{\mathbf{z}} \text{tr} \left( \rho_{A_{\text{out}}|\mathbf{z}}^2 \right) \right) \geq -2\log_2 \left( \mathbb{E}_{\text{Haar}} \mathbb{E}_{\mathbf{z}} \text{tr} \left( \rho_{A_{\text{out}}|\mathbf{z}}^2 \right) \right). \quad (\text{D5})$$

Now we start to evaluate the quantity  $\mathbb{E}_{\text{Haar}} \mathbb{E}_{\mathbf{z}} \text{tr} \left( \rho_{A_{\text{out}}|\mathbf{z}}^2 \right)$ . Through the global unitary  $U$ , the output pre-measurement state is

$$|\psi\rangle_{RA_{\text{out}}B} = (\mathbf{I}_R \otimes U) |\Phi\rangle_{RA_{\text{in}}} |0\rangle_B, \quad (\text{D6})$$

where  $|\Phi\rangle_{RA_{\text{in}}} = \frac{1}{\sqrt{d_A}} \sum_{i=0}^{d_A-1} |i\rangle_R |i\rangle_{A_{\text{in}}}$  is the maximally entangled state between  $R$  and  $A_{\text{in}}$ . Here the unitary is only applied on systems of  $A_{\text{in}}B$  as illustrated in Fig. 4a1 of the main text. Via the projective measurement on the bath  $B$ , the conditional post-measurement state is

$$|\psi_{\mathbf{z}}\rangle_{RA_{\text{out}}} = {}_B \langle \mathbf{z} | \psi_{\mathbf{z}} \rangle_{RA_{\text{out}}B} / \sqrt{p_{\mathbf{z}}}, \quad (\text{D7})$$

where  $p_{\mathbf{z}}$  is the corresponding measurement probability

$$p_{\mathbf{z}} = |\langle \psi_{\mathbf{z}} | \psi_{\mathbf{z}} \rangle_{RA_{\text{out}}}|^2 = \text{tr} (U |\Phi\rangle\langle\Phi| |0\rangle\langle 0| U^\dagger |\mathbf{z}\rangle\langle\mathbf{z}|_B). \quad (\text{D8})$$

The reduced state on  $A_{\text{out}}$  is thus

$$\rho_{A_{\text{out}}|\mathbf{z}} = \text{tr}_R (|\psi_{\mathbf{z}}\rangle\langle\psi_{\mathbf{z}}|) \quad (\text{D9})$$

$$= p_{\mathbf{z}}^{-1} \text{tr}_{RB} (U |\Phi\rangle\langle\Phi| |0\rangle\langle 0| U^\dagger |\mathbf{z}\rangle\langle\mathbf{z}|_B) \quad (\text{D10})$$

$$= p_{\mathbf{z}}^{-1} \text{tr}_B \left( U \frac{\mathbf{I}}{d_A} |0\rangle\langle 0| U^\dagger |\mathbf{z}\rangle\langle\mathbf{z}|_B \right) \equiv p_{\mathbf{z}}^{-1} \tilde{\rho}_{A_{\text{out}}|\mathbf{z}}, \quad (\text{D11})$$

where we define  $\tilde{\rho}_{A_{\text{out}}|\mathbf{z}}$  to be the unnormalized state for convenience, and thus the the measurement probability is simply  $p_{\mathbf{z}} = \text{tr}(\tilde{\rho}_{A_{\text{out}}|\mathbf{z}})$ . With those notions, we turn to the average purity defined as

$$\gamma \equiv \mathbb{E}_{\mathbf{z}} \text{tr} \left( \tilde{\rho}_{A_{\text{out}}|\mathbf{z}}^2 \right) = \sum_{\mathbf{z}} p_{\mathbf{z}}^{-1} \text{tr} \left( \tilde{\rho}_{A_{\text{out}}|\mathbf{z}}^2 \right) = \sum_{\mathbf{z}} \left[ \text{tr}(\tilde{\rho}_{A_{\text{out}}|\mathbf{z}})^{-1} \text{tr} \left( \tilde{\rho}_{A_{\text{out}}|\mathbf{z}}^{\otimes 2} \mathbb{S} \right) \right], \quad (\text{D12})$$

where  $\mathbb{S}$  is the swap operator between the two replicas. To derive  $\gamma$ , we consider the pseudo purity  $\gamma^{(m)}$  defined as

$$\gamma^{(m)} \equiv \sum_{\mathbf{z}} \text{tr}(\tilde{\rho}_{A_{\text{out}}|\mathbf{z}})^m \text{tr} \left( \tilde{\rho}_{A_{\text{out}}|\mathbf{z}}^{\otimes 2} \mathbb{S} \right) \quad (\text{D13})$$

$$= \sum_{\mathbf{z}} \text{tr} \left( \tilde{\rho}_{A_{\text{out}}|\mathbf{z}}^{\otimes(m+2)} \mathbf{I}_m \otimes \mathbb{S} \right) \quad (\text{D14})$$

$$= \sum_{\mathbf{z}} \text{tr} \left( \text{tr}_B \left( U \frac{\mathbf{I}}{d_A} |0\rangle\langle 0| U^\dagger |\mathbf{z}\rangle\langle\mathbf{z}|_B \right)^{\otimes(m+2)} \mathbf{I}_m \otimes \mathbb{S} \right) \quad (\text{D15})$$

$$= \sum_{\mathbf{z}} \text{tr} \left( U^{\otimes(m+2)} \frac{\mathbf{I}^{\otimes(m+2)}}{d_A^{(m+2)}} |0\rangle\langle 0|^{\otimes(m+2)} U^{\dagger \otimes(m+2)} \mathbf{I}_m \mathbb{S} |\mathbf{z}\rangle\langle\mathbf{z}|_B^{\otimes(m+2)} \right) \quad (\text{D16})$$

$$\equiv \text{tr} \left( U^{\otimes(m+2)} \frac{\mathbf{I}^{\otimes(m+2)}}{d_A^{(m+2)}} |0\rangle\langle 0|^{\otimes(m+2)} U^{\dagger \otimes(m+2)} (\mathbf{I}_m \otimes \mathbb{S} \otimes D_{m+2}) \right), \quad (\text{D17})$$

where again  $D_{m+2} = \sum_{\mathbf{z}} |\mathbf{z}\rangle\langle\mathbf{z}|^{\otimes(m+2)}$  as we have in Appendix C.

The Haar unitary twirling with  $m+2$  replicas is

$$\begin{aligned} \mathbb{E}_{\text{Haar}} \left[ U^{\otimes(m+2)} \otimes U^{\dagger\otimes(m+2)} \right] &= \sum_{\sigma, \pi} \text{Wg}(\sigma^{-1}\pi, m+2) |\sigma\rangle\langle\pi| \\ &= \sum_{\sigma} \text{Wg}(e, m+2) |\sigma\rangle\langle\sigma| + \sum_{\sigma \neq \pi} \text{Wg}(\sigma^{-1}\pi, m+2) |\sigma\rangle\langle\pi|, \end{aligned} \quad (\text{D18})$$

where  $\sigma, \pi$  are permutation operators from permutation group  $\mathcal{S}_{m+2}$ . As we have seen from Eq. (D17), the boundary condition is  $\tau_2 \equiv \mathbf{I}_m \otimes \mathbb{S}$  and  $D_{m+2}$  on subsystem  $A$  and  $B$  separately. The ensemble average of  $\gamma^{(m)}$  can thus be written as

$$\mathbb{E}_{\text{Haar}} \left[ \gamma^{(m)} \right] = \frac{1}{d_A^{m+2}} (e|_A \langle 0|_B \mathbb{E}_{\text{Haar}} \left[ U^{\otimes(m+2)} \otimes U^{\dagger\otimes(m+2)} \right] |\tau_2\rangle_A |D_{m+2}\rangle_B) \quad (\text{D19})$$

$$= \frac{1}{d_A^{m+2}} (e|_A \langle 0|_B \left( \sum_{\sigma} \text{Wg}(e, m+2) |\sigma\rangle\langle\sigma| + \sum_{\sigma \neq \pi} \text{Wg}(\sigma^{-1}\pi, m+2) |\sigma\rangle\langle\pi| \right) |\tau_2\rangle_A |D_{m+2}\rangle_B), \quad (\text{D20})$$

where  $(e|$  is the identity operator over  $m+2$  replicas and  $(0| = |0\rangle\langle 0|^{\otimes(m+2)}$  is the zero initial state on subsystem  $B$ . For the first part in Eq. (D20), we have

$$\begin{aligned} &\frac{1}{d_A^{m+2}} (e|_A \langle 0|_B \sum_{\sigma} \text{Wg}(e, m+2) |\sigma\rangle\langle\sigma| |\tau_2\rangle_A |D_{m+2}\rangle_B) \\ &= \frac{1}{d_A^{m+2}} (e|_A \langle 0|_B \text{Wg}(e, m+2) \sum_{\sigma} |\sigma\rangle d_A^{|\sigma^\dagger \tau_2|} d_B) \end{aligned} \quad (\text{D21})$$

$$= \frac{d_B}{d_A^{m+2}} \text{Wg}(e, m+2) \sum_{\sigma} d_A^{|\sigma^\dagger \tau_2| + |\sigma|}, \quad (\text{D22})$$

where we utilize the fact that  $(\sigma|D_{m+2}) = d_B, \forall \sigma \in \mathcal{S}_{m+2}$  to obtain Eq. (D21), and  $|\sigma|$  is again the number of cycles of permutation  $\sigma$ . The first two leading order term in the summation above is

$$\sum_{\sigma} d_A^{|\sigma^\dagger \tau_2| + |\sigma|} = d_A^{m+2+m+1} + d_A^{m+1+m+2} + \sum_{\sigma \in \mathcal{S}_{m+2} \setminus \{\tau_2, e\}} d_A^{|\sigma^\dagger \tau_2| + |\sigma|} \simeq 2d_A^{2m+3}, \quad (\text{D23})$$

where the first and second term origins from  $\sigma = \tau_2$  and  $e$ . Therefore, we can asymptotically have the first term in Eq. (D20) as

$$\frac{1}{d_A^{m+2}} (e|_A \langle 0|_B \sum_{\sigma} \text{Wg}(e, m+2) |\sigma\rangle\langle\sigma| |\tau_2\rangle_A |D_{m+2}\rangle_B) \simeq \frac{2d_A^{2m+3} d_B}{d_A^{m+2}} \text{Wg}(e, m+2) \simeq 2d_A^{-1} d_B^{-m-1}, \quad (\text{D24})$$

where we utilize  $\text{Wg}(e, m+2) \simeq 1/(d_A^{m+2} d_B^{m+2})$  in the last approximation. Similarly, we now evaluate the second term in Eq. (D20) as

$$\begin{aligned} &\frac{1}{d_A^{m+2}} (e|_A \langle 0|_B \sum_{\sigma \neq \pi} \text{Wg}(\sigma^{-1}\pi, m+2) |\sigma\rangle\langle\pi| |\tau_2\rangle_A |D_{m+2}\rangle_B) \\ &= \frac{1}{d_A^{m+2}} (e|_A \langle 0|_B \sum_{\sigma \neq \pi} \text{Wg}(\sigma^{-1}\pi, m+2) |\sigma\rangle d_A^{|\pi^\dagger \tau_2|} d_B) \end{aligned} \quad (\text{D25})$$

$$= \frac{d_B}{d_A^{m+2}} \sum_{\sigma \neq \pi} \text{Wg}(\sigma^{-1}\pi, m+2) d_A^{|\pi^\dagger \tau_2| + |\sigma|}. \quad (\text{D26})$$



The leading order terms in the summation above is

$$\begin{aligned} & \sum_{\sigma \neq \pi} \text{Wg}(\sigma^{-1}\pi, m+2) d_A^{|\pi^\dagger \tau_2| + |\sigma|} \\ &= \sum_{\sigma \neq \tau_2} \text{Wg}(\sigma^{-1}\tau_2, m+2) d_A^{m+2+|\sigma|} + \sum_{\pi \neq \tau_2} \text{Wg}(\tau_2^{-1}\pi, m+2) d_A^{|\pi^\dagger \tau_2| + m+1} + \sum_{\substack{\sigma \neq \pi \\ \sigma, \pi \neq \tau_2}} \text{Wg}(\sigma^{-1}\pi, m+2) d_A^{|\pi^\dagger \tau_2| + |\sigma|} \end{aligned} \quad (\text{D27})$$

$$\begin{aligned} &= \text{Wg}(e\tau_2, m+2) d_A^{m+2+m+2} + \sum_{\sigma \neq \tau_2, e} \text{Wg}(\sigma^{-1}\tau_2, m+2) d_A^{m+2+|\sigma|} + \text{Wg}(\tau_2^{-1}e, m+2) d_A^{m+1+m+1} \\ &+ \sum_{\pi \neq \tau_2, e} \text{Wg}(\tau_2^{-1}\pi, m+2) d_A^{|\pi^\dagger \tau_2| + m+1} + \sum_{\substack{\sigma \neq \pi \\ \sigma, \pi \neq \tau_2}} \text{Wg}(\sigma^{-1}\pi, m+2) d_A^{|\pi^\dagger \tau_2| + |\sigma|} \end{aligned} \quad (\text{D28})$$

$$\simeq -\frac{d_A^{2m+4}}{d_A^{m+3} d_B^{m+3}} - \frac{d_A^{2m+2}}{d_A^{m+3} d_B^{m+3}} + \dots \quad (\text{D29})$$

$$\simeq -d_B^{-(m+3)} (d_A^{m+1} + d_A^{m-1}), \quad (\text{D30})$$

where we utilize  $\text{Wg}(e\tau_2, m+2) \simeq -1/d_A^{m+3} d_B^{m+3}$  to obtain Eq. (D28). The second term of Eq. (D18) thus asymptotically becomes

$$\frac{1}{d_A^{m+2}} (e|_A \langle 0|_B \sum_{\sigma \neq \pi} \text{Wg}(\sigma^{-1}\pi, m+2) |\sigma\rangle \langle \pi||\tau_2\rangle_A |D_{m+2}\rangle_B) \simeq -\frac{d_B}{d_A^{m+2}} d_B^{-(m+3)} (d_A^{m+1} + d_A^{m-1}) = -(d_A^{-1} + d_A^{-3}) d_B^{-m-2}. \quad (\text{D31})$$

Therefore, the ensemble average of pseudo purity is asymptotically approximated as

$$\mathbb{E}_{\text{Haar}} [\gamma^{(m)}] \simeq 2d_A^{-1} d_B^{-m-1} - (d_A^{-1} + d_A^{-3}) d_B^{-m-2}, \quad (\text{D32})$$

and by taking the replica trick limit of  $m \rightarrow -1$ , we have

$$\mathbb{E}_{\text{Haar}} [\gamma] \simeq 2d_A^{-1} - (d_A^{-1} + d_A^{-3}) d_B^{-1} = \frac{2}{d_A} \left( 1 - \frac{1}{2d_B} - \frac{1}{2d_A^2 d_B} \right). \quad (\text{D33})$$

The expected average mutual information is thus asymptotically lower bounded by

$$\mathbb{E}_{\text{Haar}} \mathbb{E}_{\mathbf{z}} I(R : A_{\text{out}}|z) \gtrsim -2 \log_2 \left( \frac{2}{d_A} \left( 1 - \frac{1}{2d_B} - \frac{1}{2d_A^2 d_B} \right) \right), \quad (\text{D34})$$

which is exactly Lemma. 3 in the main text.

### Appendix E: Additional details on quantum circuit size

In this section, we discuss the scaling of quantum circuit size with different choices of  $N_B$  in holographic deep thermalization in detail. For convenience, we reprint the definition of quantum circuit size here

$$\text{Q-size} \equiv \text{depth per step} \times T \times (N_A + N_B) \quad (\text{E1})$$

$$\propto T \times (N_A + N_B)^2, \quad (\text{E2})$$

where the second line origins from the unitary design [10, 37].

To generate an  $\epsilon$ -approximate  $K$ -design state ensemble in holographic deep thermalization, we need  $N_B \gtrsim K + \log_2(1/\epsilon)$ . From Ineq. (4) in the main text, the minimum Q-size is

$$\text{Q-size} \propto \frac{(N_A + N_B)^2}{N_B} \times \left[ KN_A - \log_2(K!) + \log_2 \left( \frac{1}{\epsilon} \right) \right]. \quad (\text{E3})$$

Following Eq. (E3), we notice that the minimum quantum circuit size is achieved at  $N_B = N_A$  as (assuming that  $N_A \geq K + \log_2(1/\epsilon)$ )

$$\text{Q-size}|_{N_B=N_A} \gtrsim 4N_A \left[ KN_A - \log_2(K!) + \log_2 \left( \frac{1}{\epsilon - (2^K - 1)2^{-N_A}} \right) \right] \quad (\text{E4})$$

$$\sim 4KN_A^2 + 4N_A \log_2(1/K!\epsilon). \quad (\text{E5})$$

At the minimum necessary bath  $N_B = K + \log_2(1/\epsilon)$ , from the expression of the relative frame potential error,

$$\delta^{(K)} = \frac{2^K - 1}{d_B} + d_B^{-T} \frac{1}{\mathcal{F}_{\text{Haar}}^{(K)}} \simeq \frac{2^K - 1}{d_B} + d_B^{-T} \frac{d_A^K}{K!} = \epsilon, \quad (\text{E6})$$

we can solve the necessary time steps

$$T|_{N_B=K+\log_2(1/\epsilon)} = K \frac{N_A}{N_B} - \frac{1}{N_B} \log_2(K!) + 1. \quad (\text{E7})$$

Then the quantum circuit size becomes

$$\text{Q-size}|_{N_B=K+\log_2(1/\epsilon)} \propto T(N_A + N_B)^2 \quad (\text{E8})$$

$$= (KN_A - \log_2(K!) + K + \log_2(1/\epsilon)) \left( \frac{N_A}{K + \log_2(1/\epsilon)} + 1 \right) (N_A + K + \log_2(1/\epsilon)). \quad (\text{E9})$$

On the other hand, for  $T = 1$  corresponding to the conventional deep thermalization, in order to guarantee small error

$$\delta^{(K)} = \frac{1}{d_B} \left( 1 + \frac{1}{\mathcal{F}_{\text{Haar}}^{(K)}} \right) \simeq \frac{1}{d_B} \left( 1 + \frac{d_A^K}{K!} \right) \leq \epsilon, \quad (\text{E10})$$

we require

$$N_B \gtrsim \log_2 \left( 1 + \frac{d_A^K}{K!} \right) + \log_2(1/\epsilon) \simeq KN_A - \log_2(K!) + \log_2(1/\epsilon), \quad (\text{E11})$$

where the first line we utilize the result from Ref. [35], which is slightly more precise than our result. The quantum circuit size for conventional deep thermalization is

$$\text{Q-size}|_{N_B=KN_A - \log_2(K!) + \log_2(1/\epsilon)} = [(K + 1)N_A - \log_2(K!) + \log_2(1/\epsilon)]^2, \quad (\text{E12})$$

which is always a quadratic scaling in  $N_A$ .

To compare the quantum circuit size requirement in Eq. (E9) and Eq. (E12), we can analytically solve the critical  $N_A^*(K, \epsilon)$  such that their quantum circuit size is equal. To reveal the scaling of  $N_A^*(K, \epsilon)$  explicitly, we have

$$(KN_A - \log_2(K!) + K + \log_2(1/\epsilon)) \frac{(N_A + K + \log_2(1/\epsilon))^2}{K + \log_2(1/\epsilon)} = ((K + 1)N_A - \log_2(K!) + \log_2(1/\epsilon))^2 \quad (\text{E13})$$

$$(KN_A - K + K + \log_2(1/\epsilon)) \frac{(N_A + K + \log_2(1/\epsilon))^2}{K + \log_2(1/\epsilon)} = ((K + 1)N_A + \log_2(1/\epsilon))^2 \quad (\text{E14})$$

$$N_A^*(K, \epsilon) \simeq \frac{1}{2} \left( \sqrt{(K + \log_2(1/\epsilon)) (K^3 + K^2 \log_2(1/\epsilon) + 4 \log_2(1/\epsilon))} + K^2 + K \log_2(1/\epsilon) \right) \quad (\text{E15})$$

where in the second line we take  $\log_2(K!) \rightarrow K$  in the L.H.S and get rid of the one in R.H.S. for convenience. Eq. (E15) indicates that the critical system size  $N_A^*(K, \epsilon)$  undergoes a continuous transition from approximation-error-dependent scaling  $\sim K \log_2(1/\epsilon)$  to universal scaling  $K^2$  with increasing order  $K$  shown in Fig. 8, and we can roughly estimate the transition point to be  $K \sim \log_2(1/\epsilon)$ . The threshold can be summarized as

$$N_A^*(K, \epsilon) = \begin{cases} K \log_2(1/\epsilon), & \text{if } K \ll \log_2(1/\epsilon); \\ K^2, & \text{if } K \gg \log_2(1/\epsilon). \end{cases} \quad (\text{E16})$$

When  $N_A \geq N_A^*(K, \epsilon)$ , the minimum bath case requires higher quantum circuit size, otherwise conventional deep thermalization requires higher quantum circuit size.

In the following, we analyze the scaling of quantum circuit size with  $K \leq \log_2(1/\epsilon)$ .

For  $K < \log_2(1/\epsilon)$ , the quantum circuit size of minimum bath scales as

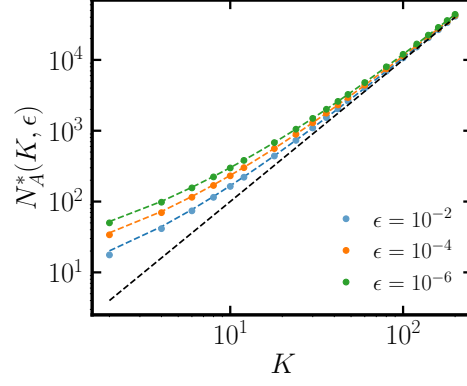


Figure 8. The critical system size  $N_A^*(K, \epsilon)$  for quantum circuit size with minimum bath equals conventional deep thermalization. Colored dots represent  $N_A^*(K, \epsilon)$  with different  $\epsilon$ . Colored dashed lines represent the solution from Eq. (E15) with corresponding  $\epsilon$ , and black dashed line indicate the scaling of  $\sim K^2$ .

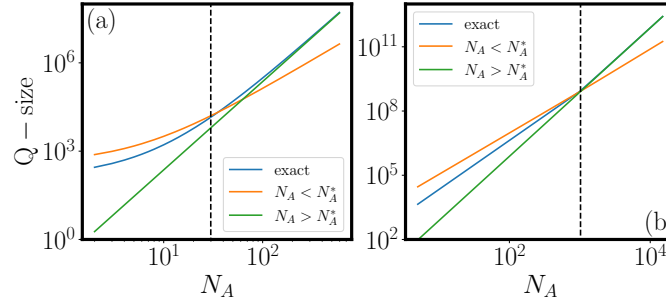


Figure 9. The scaling of quantum circuit size with minimum bath for (a)  $K < \log_2(1/\epsilon)$  and (b)  $K > \log_2(1/\epsilon)$ . Parameters:  $\epsilon = 10^{-3}$ ; (a)  $K = 3$  (b)  $K = 32$ . Blue lines show exact result in Eq. (E9). Orange lines represent scaling analyses as (a)  $(K+1)(KN_A + \log_2(1/\epsilon))(N_A + \log_2(1/\epsilon))$  and (b)  $K^3(N_A + 1 - \log_2(K))(N_A + K)/(K + \log_2(1/\epsilon))$ . The green lines represent  $KN_A^3/(K + \log_2(1/\epsilon))$ . Black vertical dashed lines indicate (a)  $N_A^* \sim K \log_2(1/\epsilon)$  and (b)  $N_A^* \sim K^2$ .

1.  $N_A < N_A^* = K \log_2(1/\epsilon)$ . Q-size  $\simeq (K+1)(KN_A + \log_2(1/\epsilon))(N_A + \log_2(1/\epsilon))$ .
2.  $N_A > N_A^* = K \log_2(1/\epsilon)$ . Q-size  $\simeq \frac{KN_A^3}{K + \log_2(1/\epsilon)}$ .

On the other hand for  $K > \log_2(1/\epsilon)$ , the quantum circuit size of minimum bath scales as

1.  $N_A < N_A^* = K^2$ . Q-size  $\simeq (KN_A - \log_2(K!) + K) \frac{K^2}{K + \log_2(1/\epsilon)} (N_A + K) \simeq \frac{K^3}{K + \log_2(1/\epsilon)} (N_A + 1 - \log_2 K)(N_A + K)$ .
2.  $N_A > N_A^* = K^2$ . Q-size  $\simeq \frac{KN_A^3}{K + \log_2(1/\epsilon)}$ .

where we apply  $\log_2(K!) \simeq K \log_2(K)$  in the first line. We demonstrate the above scalings in Fig. 9a and b for the two cases of  $K \lesseqgtr \log_2(1/\epsilon)$  separately.

In the end, we compare the scaling analysis of quantum circuit size with numerics for three cases of interest illustrated in Fig. 3c in the main text: minimum bath HDT, minimum Q-size HDT and conventional DT. In Fig. 10a with large system  $N_A \gg K \log_2(1/\epsilon)$ , Q-size of the minimum Q-size HDT (orange dots) and DT (green dots) grows quadratically with the system size  $N_A$ , though reduces circuit size requirement by a  $K$ -dependent constant. However, for minimum bath HDT, its Q-size grows cubically with  $N_A$ . The numerical results agree with our theory analyses (dashed lines) summarized in Fig. 3c in the main text. On the other hand, for relative small system  $N_A \ll K \log_2(1/\epsilon)$ , the minimum Q-size (orange) and conventional DT (green) remain quadratic growth with  $N_A$ , shown Fig. 10b. However, the minimum bath case (blue) undergoes a continuous transition from quadratic toward cubic growth and requires smaller necessary resources compared to conventional DT.

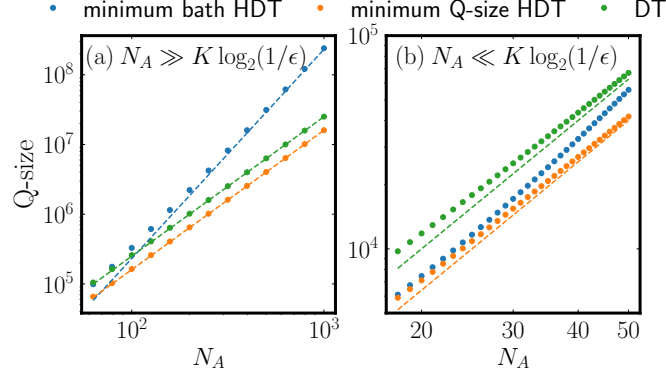


Figure 10. Scaling of Q-size for (a) large and (b) small system. In (a) we choose  $K = 4$  and  $\epsilon = 10^{-4}$  with bath size specified namely  $N_B = 17, N_A, 4N_A + 13$  for minimum bath HDT, minimum Q-size HDT and conventional DT. Dots are numerically solved. Orange and green dashed lines in (a)-(b) represent scaling of  $4KN_A^2$  and  $(K + 1)^2 N_A^2$ . Blue dashed line in (a) represent  $KN_A^3/(K + \log_2(1/\epsilon))$ .

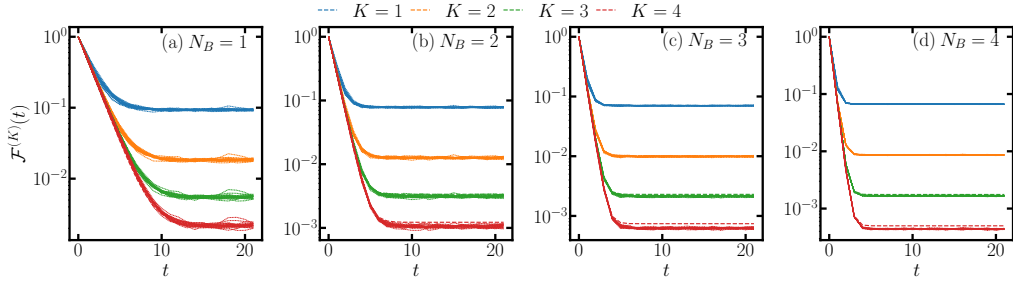


Figure 11. Dynamics of frame potential  $\mathcal{F}^{(K)}$  with different  $K$  in a system of  $N_A = 4$  and  $N_B = 1, 2, 3, 4$  (from left to right). Thin dashed lines represent the dynamics of frame potential with each sequence of randomly sampled Haar unitaries, and the thick dashed line show corresponding theoretical prediction in Eq. (2) ( $K = 1$ ) and Eq. (3) ( $K > 1$ ) in the main text.

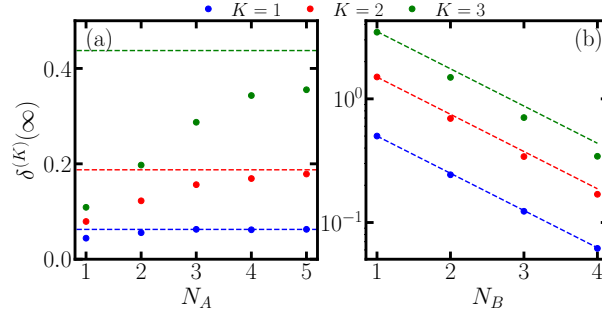


Figure 12. Relative deviation of converged frame potential  $\delta^{(K)}(\infty) = \mathcal{F}^{(K)}(\infty)/\mathcal{F}_{\text{Haar}}^{(K)} - 1$ . The system consists of (a)  $N_B = 4$  bath qubits with various  $N_A$  data qubits and (b)  $N_A = 4$  data qubits with various  $N_B$  bath qubits. Dots represents numerical simulation results and dashed lines represent theoretical prediction in Eq. (2) (blue) and Eq. (3) in the main text (red and green) as  $(2^K - 1)/d_B$ . Each dot is an average over 50 Haar unitaries realizations with ensemble of  $5 \times 10^4$  samples at step  $T = 32$ . Here we take the empirical  $\mathcal{F}_{\text{Haar}}^{(K)}$  by averaging over 50 ensembles of  $5 \times 10^4$  Haar random states to reduce the finite size effect.

## Appendix F: Additional numerical details

In this section, we provide additional details on the numerical simulation results. In Fig. 11, we present the dynamics of the frame potential of *projected ensemble* with each Haar unitary implementation in detail. Considering the different random unitary initialization (thin dashed lines), we see they agree with the theoretical prediction for ensemble average though with small fluctuations, indicating the Haar ensemble theory can well capture the dynamics

for a typical realization of random unitaries in HDT.

We further show the relative deviation of converged frame potential  $\delta^{(K)}(\infty) = \mathcal{F}^{(K)}(\infty)/\mathcal{F}_{\text{Haar}}^{(K)} - 1$  versus  $N_A$  and  $N_B$ , which is a direct measure on the approximation error to  $K$ -design. In Fig. 12a, given a bath of  $N_B$  qubits, the relative deviation (dots) saturates towards a constant (dashed lines) independent of data system size  $N_A$ , though increases with  $K$  due to stronger randomness necessities. Meanwhile, increasing the bath system size can reduce the deviation exponentially in Fig. 12b as we have seen in Fig. 2 of the main text. Overall, the numerical results supports our empirical result in Eq. (3) of the main text.

### Appendix G: Additional details on quantum machine learning

In this section, we provide additional details on the loss function and circuit design in the QML-enhanced HDT.

We have chosen the interpolated loss function

$$\mathcal{L}_t(\rho_t) = (1 - \tau_t)(1 - F_{\text{sup}}(\rho_t, |\psi_0\rangle)) + \tau_t(1 - F_{\text{sup}}(\rho_t, \mathbf{I}/d_A)), \quad (\text{G1})$$

where  $\rho_t$  is the average state at step  $t$  and  $\mathbf{I}/d_A$  is the maximally mixed state on the  $N_A$  data qubit. We adopt the *superfidelity* [38] for efficient evaluation in training without significant impact on performance

$$F_{\text{sup}}(\rho, \sigma) = \text{tr}(\rho\sigma) + \sqrt{(1 - \text{tr}\rho^2)(1 - \text{tr}\sigma^2)}. \quad (\text{G2})$$

Specifically, for the two states  $|\psi_0\rangle$  and  $\mathbf{I}/d_A$  considered in loss function, the *superfidelity* can be further simplified to  $F_{\text{sup}}(\rho_t, |\psi_0\rangle) = \langle\psi_0|\rho_t|\psi_0\rangle$  and  $F_{\text{sup}}(\rho_t, \mathbf{I}/2^N) = 1/d_A + \sqrt{(d_A - 1)(1 - \text{tr}\rho_t^2)/d_A}$ . Therefore, one can regard the loss function in Eq. (G1) as a nonlinear scheduling on the decay of purity of  $\rho_t$  towards  $1/d_A$ . The loss function considered here is also closed connected to the MMD distance in QuDDPM [33].

Note that utilizing the average-state-dependent loss function avoids the precise control and tracking of measurement results on ancillary qubits, though a Monte-Carlo sampling error exists due to finite sampling. In particular, both  $\langle\psi_0|\rho_t|\psi_0\rangle$  and  $\text{tr}(\rho_t^2)$  are experimental tractable to measure. For the purity measure, one can either run two quantum devices simultaneously to obtain two copies of the average state, and then estimate the purity via a control-SWAP circuit with an extra control qubit. Another recent proposed option relies on the random measurement toolbox, e.g., classical shadow [8]. For the control-SWAP circuit, it requires the application of a global control-SWAP gate on the two copies of  $N$ -qubit state conditioned on control qubit's state, which can be decomposed into  $N$  control-SWAP gates applied on two qubits only. In comparison, classical shadow only requires an extra layer of random single qubit Pauli gate for efficient estimation, though at the cost of more random measurements.

In each step, we parameterize the unitary via a hardware-efficient ansatz [32] where each layer of circuit involves single qubit X and Y rotations followed by control-Z gates in brickwall fashion. In numerical simulation, we choose  $L = 2(N_A + N_B)$  layers for each step.

### Appendix H: Additional details on experiment

In this section, we provide additional details on the IBM Quantum experiments. In Fig. 13a-c, we show the result of first-order frame potential for each choice of randomly selected circuit parameters (grey dashed lines). Within the fluctuations due to finite system size and randomly selected parameters, the decay of  $\mathcal{F}^{(1)}(T)$  versus  $N_B$  and  $T$  is well captured by the Haar ensemble average results.

---

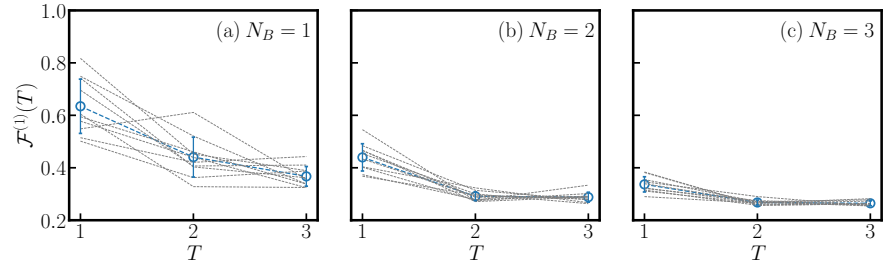


Figure 13. Decay of first order frame potential in a system of  $N_A = 2$  data qubits and various  $N_B$  bath qubits versus time steps  $T$  of IBM Quantum Brisbane. Grey dashed line represent result with each set of parameters. Blue circles with errorbars show the mean and standard deviation.